TEXAS CHRISTIAN UNIVERSITY

Nonlinear Dynamics of Two and Three Dimensional Gravitational Billiard Systems

by

Cameron K. Langer

A thesis submitted in partial fulfillment for
Departmental Honors in Physics

in the
Department of Physics and Astronomy
Texas Christian University
Fort Worth, Texas

May 2015

Nonlinear Dynamics of Two and Three Dimensional Gravitational Billiard Systems

Project Approved:

Supervising Professor: Bruce N. Miller, Ph.D.
Department of Physics and Astronomy

Susan Staples, Ph.D.
Department of Mathematics

Paul Lawrence, Ph.D.
Department of Physics and Astronomy

TEXAS CHRISTIAN UNIVERSITY

Abstract

Thesis Advisor: Bruce N. Miller
Department of Physics and Astronomy

Departmental Honors in Physics

by Cameron K. Langer

One of the prime paradigms of nonlinear dynamics, billiard systems offer a simple setting to examine regular and chaotic motion. Gravitational billiards are generalizations of classical billiards ideal for both analytical and experimental investigations. In this thesis, we study the nonlinear dynamics of two natural generalizations of one of the most widely studied Hamiltonian gravitational billiards, the wedge billiard. First, we incorporate time-dependence into the system through sinusoidal driving of the wedge. We introduce a model describing the driven wedge in terms of a four-dimensional discrete map, and analyze the properties of this map analytically and numerically. Unbounded orbits in the form of Fermi acceleration are confirmed for elastic collisions, and regular and chaotic attractors are found for inelastic collisions. Next, we examine the natural three-dimensional generalization of the wedge billiard: the conic billiard. Namely, we consider the motion of a classical particle in a constant gravitational field, colliding elastically with a linear cone of vertex angle 2θ. We derive a two-dimensional area-preserving map characterizing the dynamics, and demonstrate several integrable limits of the system. We compute some simple periodic orbits and analyze their stability as a function of parameters, and present some additional numerical results. We find that for small values of ℓ_z, the z-component of angular momentum, the conic billiard exhibits behavior characteristic of two-degree-of-freedom Hamiltonian systems with a discontinuity, and the dynamics are qualitatively similar to that of the wedge billiard. As we increase ℓ_z the dynamics become less chaotic, and the correspondence with the wedge billiard is lost.

Acknowledgements

First, I would like to sincerely thank my advisor, Dr. Bruce N. Miller for all of his help and guidance. Next, I would like to thank my committee members, Dr. Susan Staples and Dr. Paul Lawrence. Finally, I would like to acknowledge the faculty in the Department of Physics and Astronomy for their support throughout my time at Texas Christian University.

Contents

List of Figures

Chapter 1

Introduction

1.1 Historical Remarks

One of the most popular tools used for investigating aspects of nonlinear dynamics, classical billiards offer a setting in which the dynamics is both conceptually and computationally tractable. First introduced by Birkhoff in [1], a *dynamical billiard* is defined as the motion of a point mass (the "billiard" or "particle") in a region with a piecewise smooth boundary, where the motion between collisions is inertial and collisions with the boundary are specular and elastic. The natural way to study these systems is using a *Poincaré surface of section* (see Appendix A) taken at encounters with the boundary. Depending on the nature of the boundary, the motion of the billiard can be regular or chaotic. While these classical billiards are optimal for analytical study, more experimentally approachable models accounting for the Earth's gravitational field, called *gravitational billiards*, have also been widely studied. The first such model, called the *gravitational bouncer*, consists of a particle colliding with a periodically driven boundary in the presence of a constant gravitational field. This system was introduced as a variant of the "Fermi piston," which was introduced by Ulam [2] as a simple analog of a mechanism first suggested by Fermi [3] in the study of the origins of high-energy cosmic rays. Originally, it was thought that for a particle colliding elastically between one fixed

and one oscillating wall, the average velocity of the particle would reach arbitrarily large values after sufficiently long times. Investigations by Pustyl'nikov in [4–6] showed that although in the Fermi-Ulam model energy remained bounded for sufficiently smooth wall motions, unbounded orbits could be found in the related gravitational bouncer. Investigations into the presence and nature of orbits in which a classical particle experiences unbounded energy gain (*Fermi acceleration*) have been carried out from both analytical and numerical perspectives for numerous systems. Recent work on the elastic bouncer [7, 8] and Fermi-Ulam [9] models has examined the transport properties of the phase space and the role of phase transitions in Fermi acceleration. For the bouncer model, early studies [10–13] examined simplified versions of the system and introduced energy loss in collisions, with more recent work [14, 15] focusing on the chaotic dynamics and strange attractors observed in the inelastic system. Additionally, the phenomenon known as *inelastic collapse* [16, 17], where a particle completes an infinite number of collisions in a finite time, plays a significant role in the inelastic system. While some open questions remain, the generic features of this one-dimensional sinusoidally driven dynamical system are fairly well understood.

Gravitational billiards have also been studied in two dimensions. In [18], the *wedge billiard*, consisting of a particle falling between two symmetric linear boundaries (the "wedge") of angle 2θ, was shown to exhibit the full range of possible behavior in Hamiltonian systems with two degrees of freedom. Namely, for $\theta < 45°$ the phase space consists of a mixed phase space with regular and chaotic regions, for $\theta = 45°$ the system is integrable, and for $\theta > 45°$ the system is ergodic. Subsequent work on the wedge billiard includes [19] where the oscillations in the relative amount of chaotic versus regular parts of the phase space (the so-called "breathing chaos") are discussed in terms of the symmetry lines of the system, and [20] where the ergodicity of the wedge for $\theta > 45°$ is rigorously established. Other two-dimensional gravitational billiards include the parabolic billiard, which is completely integrable [21], and the hyperbolic billiard,

which includes the behavior of both the wedge and parabolic systems for different parameter values [22]. Recently, the *driven* versions of these three billiard systems were studied experimentally in [23] and numerically in [24]; in the latter study, rotational effects were included in the theoretical model. In both of these works, a horizontal ceiling was placed to limit the height of the billiard. This has a significant effect on the dynamics, and thus it is natural to inquire as to what happens to the "purely" driven wedge i.e., when there is no ceiling. These types of systems, broadly classified as *time-dependent two-dimensional billiards*, have been the subject of recent study [25–27] for both elastic and inelastic collisions. In the elastic case, several interesting behaviors can arise e.g., Fermi acceleration for time-dependent perturbations to the (integrable) elliptic billiard [25].

One possible issue with experiments conducted on the driven wedge is the two-dimensional nature of the idealized system. In the real system, the billiard is not a point particle and thus has rotational properties which are affected at each collision. In the experiments of Feldt et al in [23], additional boundaries were used to ensure the motion of the billiard was contained in the plane; however, any collision with these boundaries would likely play a nontrivial role in the dynamics. One way of eliminating this problem would be to get rid of the constraint that the motion be contained in a plane. If, instead of a particle in a wedge, we considered a particle in a *cone*, then there would be no need for additional boundaries. In fact, such a system would be ideal for studying the effects of rotation on billiard systems, as the cone could either be driven in the conventional sense (i.e., the entire cone oscillating in a fixed direction) *or* the cone could spin in a sinusoidal fashion. As the equations determining the time of the next collision are in a sense unaffected by this "rotational" driving, such a system might still be analytically feasible, while also being experimentally realizable.

1.2 Objectives of this Work

In this work, we are concerned with the nonlinear dynamics of two distinct systems which arise as extensions of the wedge billiard: (i) the sinusoidally driven, dissipative wedge, and (ii) the three-dimensional generalization of the wedge, the conic billiard.

1.2.1 The Driven Wedge

In the first part of this thesis, we investigate the nonlinear dynamics of the driven wedge billiard. That is, we consider the motion of a classical particle under the influence of a constant gravitational field, colliding with two linear boundaries which oscillate sinusoidally in time. After defining the system, we derive a four-dimensional Poincaré map describing the dynamics, and analyze some basic properties of this map analytically. We derive some simple fixed point solutions and study their stability analytically and numerically as a function of parameter values. We then describe a numerical method of computing the time of the next collision which avoids the problem of multiple roots, a feature present in the one-dimensional Fermi piston. With this algorithm, we explore the phase space of the driven wedge numerically. Since the phase space is four-dimensional, we utilize projections and slices of the phase space to visualize the dynamics. For elastic collisions, we find that for small oscillations the structures in the phase space of the static wedge billiard are preserved. That is, the qualitative behavior survives small perturbations. As the strength of oscillation is increased, Fermi acceleration emerges in addition to periodic and quasiperiodic behavior. For inelastic collisions, there are two competing mechanics at work: namely, the energy gain due to the driven boundary which accelerates the particle, and energy loss due to collisions in the form of a constant restitution coefficient. As expected, for certain parameter values we find that these processes balance and give rise to regular and chaotic attractors which dominate the phase space. In addition to these attractors, a two-dimensional version of inelastic

collapse is present, where the particle completes a large number of collisions near the vertex of the wedge.

1.2.2 The Conic Billiard

In the second part of this work, we introduce the *conic billiard*, which is a three-dimensional generalization of the wedge. More precisely, we consider the motion of a particle in a constant gravitational field, colliding elastically with a *static* linear cone which makes an angle θ with the positive z-axis. Here we consider only elastic collisions, so that energy is conserved. Using an additional constant of the motion (the z-component of angular momentum), we demonstrate that the system can be reduced to the study of a two-dimensional area-preserving map with two parameters. We derive this map, study some of its simple properties, and show that the conic billiard possesses several integrable limits. We compute the fixed point solutions of the conic system, and analyze their stability as a function of the parameters. We then investigate the global dynamics of the system numerically, demonstrating that the choice of parameter values determines periodic, KAM, and chaotic regions in the phase space.

The final chapter of this work contains a summary of the main results on both the driven wedge and the conic billiard, as well as an outlook and prospective future directions of research.

Chapter 2

The Driven Wedge

2.1 The Wedge Billiard

The wedge billiard, first introduced in [18], consists of a classical particle under the influence of a constant gravitational field, colliding elastically with a wedge boundary of half-angle ϕ. Between collisions, the Hamiltonian of the system is (here and in the rest of this paper, we set $m = 1$ without loss of generality)

$$H = \frac{\boldsymbol{p}^2}{2} + gz, \tag{2.1}$$

where $\boldsymbol{p}$ is the particle's linear momentum, g is the gravitational acceleration, and z is the usual Cartesian co-ordinate. By suitable transformation of the time and spatial co-ordinates, we set $E = g = \frac{1}{2}$ so that energy conservation can be expressed as

$$1 = v_\perp^2 + v_\parallel^2 + z, \tag{2.2}$$

where $v_\perp$ and $v_\parallel$ are the components of the particle's velocity orthogonal and parallel to the wedge surface, respectively. The Poincaré map is represented by two maps: T_a, which corresponds to re-collisions where the particle impacts the same boundary as the previous collision, and T_b, where the collision is with the opposite boundary. In [18]

these transformations are shown to be

$$T_{\mathrm{a}} : \begin{pmatrix} v_{\parallel_{n+1}} \\ v_{\perp_{n+1}} \end{pmatrix} = \begin{pmatrix} v_{\parallel_n} - 2\cot\phi\, v_{\perp_n} \\ v_{\perp_n} \end{pmatrix}, \tag{2.3}$$

and

$$T_{\mathrm{b}} : \begin{pmatrix} v_{\parallel_{n+1}} \\ v^2_{\perp_{n+1}} \end{pmatrix} = \begin{pmatrix} \cot\phi(v_{\perp_n} - v_{\perp_{n+1}}) - v_{\parallel_n} \\ 2\sin^2\phi + 2\cos^2\phi\cos 2\phi(v_{\perp_n} - \tan\phi\, v_{\parallel_n}) - v^2_{\perp_n} \end{pmatrix}. \tag{2.4}$$

It may be shown that this map preserves the invariant measure $\mathrm{d}v_{\parallel}\,\mathrm{d}v^2_{\perp}$. This map possesses many interesting properties, many of which are summarized in [18, 19]. Here we state only the most general features of the wedge:

- For $0° < \phi < 45°$, the phase space is mixed, with coexisting stable and chaotic behavior.
- For $\phi = 0°, 45°$ and $\phi = 90°$, the system is integrable. In the limit $\phi \to 0$ the potential becomes central, at 45° new co-ordinates render the Hamiltonian separable, and at 90° the vertical and horizontal motions decouple.
- For $\phi > 45°$, the system is ergodic (see [20] for a proof).

Several generalizations of the wedge billiard have been studied from various perspectives; in [21, 22] parabolic and hyperbolic boundaries were studied, and driven versions of these three systems were studied experimentally in [23] and analytically in [24, 28]. Previous analytical work on the driven wedge has focused on constructing real-world models which account for rotational and aerodynamic drag effects on the billiard's motion, in order to more closely match experimental results. This makes the construction of an iterative, "event-driven" Poincaré map more difficult. On the other hand, models of driven, two-dimensional billiard systems which neglect rotation and drag are interesting in their own right and have been studied for both elastic and inelastic collisions. Most work [2–8, 10, 11, 13, 15] on these *time-dependent billiards* has focused on one-dimensional variants of

the "Fermi piston," wherein a particle is bounded by below by an oscillating boundary and from above by either a constant gravitational field or a static boundary. In these $1 + \frac{1}{2}$ degree-of-freedom systems, the dynamics is characterized by a two-dimensional map. In two dimensions, recent investigations [25–27] have examined time-dependent versions of the elliptical, oval, and circular billiards. In general, such systems possess a four-dimensional Poincaré map. Here we introduce a simplifed model of the driven wedge, where the only "perturbation" to the original wedge system is the introduction of sinusoidal driving of the boundary. That is, we neglect all rotational effects, as well as aerodynamic drag and the vertical ceiling used in both the original experiment [23] and previous analytical work [24, 28].

2.2 The Model and the Mapping

We define the static position of the wedge boundary at time $t = 0$ as

$$y_{\mathrm{w}}(x) = m|x|, \tag{2.5}$$

where $m = \cot\phi$ is the slope of the wedge, and ϕ is the wedge half-angle. We introduce the time-dependence of the boundary by perturbing the x co-ordinates of the boundaries $x(t) = \bar{x} + f(t)$, where $f(t) = A\sin\omega t$ is a sinusoidal driving function of amplitude A and frequency ω, and $\bar{x}$ denotes the "static position" of the boundary i.e., the "x" in (2.5). Our definitions are made clear by examining Fig. 2.1 and Fig. 2.2; the former demonstrates how the location of the wedge changes as a function of time, and the latter defines the co-ordinate systems we use.

The system naturally leads to a mapping taking the billiard's position and velocity at the n^{th} collision to that at the $n + 1^{\mathrm{st}}$ collision. This mapping requires one time co-ordinate, one spatial co-ordinate (because at the moment of collision, the y co-ordinate is determined by the $\bar{x}$ co-ordinate), and two components of the billiard's velocity. We could choose the tangential and normal components of the billiard's velocity; however,

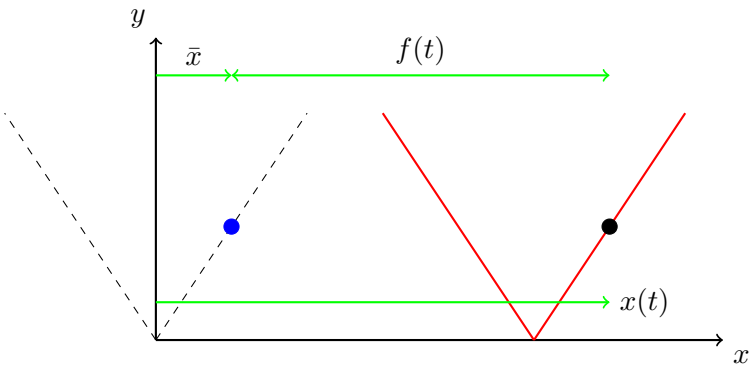

FIGURE 2.1: Diagram illustrating the time-dependence of the wedge boundary. The x-coordinate on the wedge at any time t may be written as $x = \bar{x} + f(t)$ i.e., a sum of the corresponding 'static' wedge position $\bar{x}$ and the value of the driving function $f(t)$.

in this case, since the time-of-collision map is more simple in the usual Cartesian xy-frame, we choose the x and y components of the billiard's velocity. Hence, our desired mapping is of the form

$$\mathcal{P} : (t_n, \bar{x}_n, v_{n_x}, v_{n_y}) \longrightarrow (t_{n+1}, \bar{x}_{n+1}, v_{n+1_x}, v_{n+1_y}). \tag{2.6}$$

Computing this map requires two ingredients: the time-of-collision map determining t_{n+1}, and the collision map taking the pre-collision velocities (v_x^-, v_y^-) to the post-collision velocities (v_x^+, v_y^+). The former is defined implicitly by

$$v_{n_x}(t_{n+1} - t_n) + \bar{x}_n + f(t_n) = \bar{x}_{n+1} + f(t_{n+1}), \tag{2.7}$$

$$-\frac{g}{2}(t_{n+1} - t_n)^2 + v_{n_y}(t_{n+1} - t_n) + y_n = y_{n+1}, \tag{2.8}$$

and the latter by (in the comoving frame of the boundary, see Fig. 2.2)

$$v_\parallel^+ = v_\parallel^-, \qquad\qquad v_\perp^+ = -\epsilon v_\perp^-, \tag{2.9}$$

where ϵ denotes the coefficient of restitution, y_i denotes the y co-ordinate of the billiard at the i^{th} collision (for each boundary, y_i is a function only of $\bar{x}_i$), and $v_\parallel, v_\perp$ are the components of the billiard's velocity tangential and normal to the wedge, respectively.

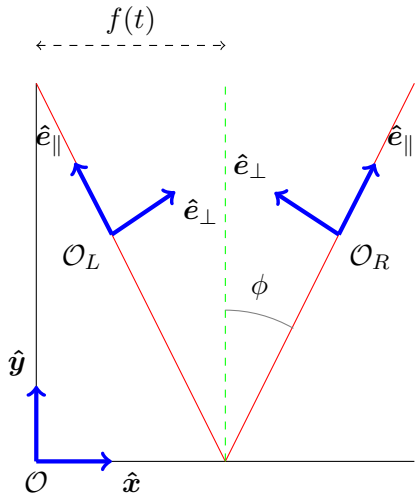

FIGURE 2.2: The system geometry and the various reference frames used, shown at a time $t \neq 0$, where the horizontal position of the wedge is perturbed to the right by $f(t)$. For clarity, the rotated frames $\mathcal{O}_{L/R}$ have been drawn higher than the translated frame $\mathcal{O}'$; in actuality these frames share the origin at the vertex of the wedge. Note that the leftmost point of the wedge need not align with the y axis.

The collision equations may be rewritten in the static Cartesian frame by a rotation and a translation of the Cartesian co-ordinate system; the results are

$$v_x^+ = \begin{cases} [\sin^2\phi - \epsilon\cos^2\phi]v_x^- + \frac{1}{2}(\epsilon+1)\sin 2\phi\, v_y^- + (\epsilon+1)\dot{f}(t_{n+1})\cos^2\phi, & R \\ [\sin^2\phi - \epsilon\cos^2\phi]v_x^- - \frac{1}{2}(\epsilon+1)\sin 2\phi\, v_y^- + (\epsilon+1)\dot{f}(t_{n+1})\cos^2\phi, & L \end{cases}, \quad (2.10)$$

$$v_y^+ = \begin{cases} \frac{1}{2}(\epsilon+1)\sin 2\phi\, v_x^- + [\cos^2\phi - \epsilon\sin^2\phi]v_y^- - \frac{1}{2}(\epsilon+1)\dot{f}(t_{n+1})\sin 2\phi, & R \\ -\frac{1}{2}(\epsilon+1)\sin 2\phi\, v_x^- + [\cos^2\phi - \epsilon\sin^2\phi]v_y^- + \frac{1}{2}(\epsilon+1)\dot{f}(t_{n+1})\sin 2\phi, & L \end{cases}, \quad (2.11)$$

where R denotes a collision with the right side of the boundary and L a collision with the left side of the boundary. In each of the three boundary types, to solve for t_{n+1} we proceed as follows. We use (2.7) to eliminate $\bar{x}_{n+1}$ in (2.8), using the relation $y_i = m|\bar{x}_i|$; this gives a single equation involving only t_{n+1} which can (in principle) be solved for the time of the next collision. The resulting equation can be separated into two cases, corresponding to collisions with the right and left sides of the boundary. The equation(s) determining the time of the $n+1^{\text{st}}$ collision can be written as (where we have defined

$\Delta t_{n+1} \equiv t_{n+1} - t_n$)

$$-\frac{g}{2}\Delta t_{n+1}^2+(v_{n_y}-mv_{n_x})\Delta t_{n+1}+m(|\bar{x}_n|-\bar{x}_n)-mA(\sin\omega t_n-\sin\omega t_{n+1})=0, \quad \bar{x}_{n+1}>0, \tag{2.12}$$

$$-\frac{g}{2}\Delta t_{n+1}^2+(v_{n_y}+mv_{n_x})\Delta t_{n+1}+m(|\bar{x}_n|+\bar{x}_n)+mA(\sin\omega t_n-\sin\omega t_{n+1})=0, \quad \bar{x}_{n+1}<0. \tag{2.13}$$

If we define the dimensionless variables

$$\tau \equiv \frac{t}{t'}, \qquad \xi \equiv \frac{\bar{x}}{x'}, \qquad u_x \equiv \frac{v_x}{v_x'}, \qquad u_y \equiv \frac{v_y}{v_y'}, \tag{2.14}$$

choose

$$x' \equiv \frac{g}{2m\omega^2}, \qquad v_x' \equiv \frac{g}{2m\omega}, \qquad v_y' \equiv \frac{g}{2\omega}, \tag{2.15}$$

as our scaling constants, and define the 'driving strength' parameter

$$\Gamma \equiv \frac{A\omega^2}{g}, \tag{2.16}$$

then the Poincaré surface-of-section mapping

$$\mathcal{P} : (\tau_n, \xi_n, u_{n_x}, u_{n_y}) \to (\tau_{n+1}, \xi_{n+1}, u_{n+1_x}, u_{n+1_y}) \tag{2.17}$$

describing the system can be written as

$$\begin{aligned}
&-\Delta\tau_{n+1}^2+\left(u_{n_y}\mp u_{n_x}\right)\Delta\tau_{n+1}+|\xi_n|\mp\xi_n\mp 2m\Gamma\left(\sin\tau_n-\sin\tau_{n+1}\right)=0,\\
\xi_{n+1} &= u_{n_x}\Delta\tau_{n+1}+\xi_n+2m\Gamma(\sin\tau_n-\sin\tau_{n+1}),\\
u_{n+1_x} &= [\sin^2\phi-\epsilon\cos^2\phi]u_{n_x}\pm(\epsilon+1)\cos^2\phi\left[-2\Delta\tau_{n+1}+u_{n_y}\right]+2\Gamma(\epsilon+1)\cos\tau_{n+1}m\cos^2\phi,\\
u_{n+1_y} &= \pm(\epsilon+1)\sin^2\phi\,u_{n_x}+[\cos^2\phi-\epsilon\sin^2\phi][-2\Delta\tau_{n+1}+u_{n_y}]\mp\Gamma(\epsilon+1)\cos\tau_{n+1}\sin 2\phi,
\end{aligned} \tag{2.18}$$

where the upper signs denote collisions with the right boundary, the lower signs denote collisions with the left boundary, we have defined

$$\Delta\tau_{n+1} \equiv \tau_{n+1} - \tau_n \tag{2.19}$$

and abbreviated $\cot\phi = m$ for clarity.

2.3 Periodic Orbits

In this section, we analyze the mapping for fixed points. For the driven wedge, the simplest possible periodic motions are the so-called *symmetric* periodic orbits where the particle hits the boundary at equal heights and opposite horizontal positions about the wedge vertex, with the x component of the velocity differing in sign at each collision. Without loss of generality consider the following sequence of collisions: the particle collides with the right boundary moving left at the n^{th} collision, and with the left boundary moving right at the $n+1^{\text{st}}$ collision. Imposing the constraint that the wedge should occupy a symmetric position about the origin at the time of consecutive collisions leads us to $\tau_{n+1} = \tau_n + k\pi$, where $k = 1, 3, 5, \ldots$. If we use this result in the first two equations in (2.18) we arrive at

$$k\pi u_{n_x} + 2\xi_n + 4\Gamma\cot\phi\sin\tau_n = 0, \qquad \text{and} \qquad -(k\pi)^2 + u_{n_y}(k\pi) = 0. \tag{2.20}$$

The latter equation implies that $u_{n_y} = k\pi$; using this in the velocity mapping for $u_{n+1_x} = -u_{n_x}$ and $u_{n+1_y} = u_{n_y}$ we find a system of linear equations for u_{n_x}, u_{n_y}, with solution

$$u_{n_x} = -\frac{2\Gamma(1+\epsilon)}{1-\epsilon}\cos\tau_n\cot\phi\cos^2\phi, \qquad u_{n_y} = \frac{2\Gamma(1+\epsilon)}{1-\epsilon}\cos\tau_n\sin\phi\cos\phi. \tag{2.21}$$

Finally, using this expression for u_{n_x} and u_{n_y} in (2.20), we complete our fixed point solution:

$$\tau_n = \arccos\left(\frac{k\pi(1-\epsilon)}{\Gamma(1+\epsilon)}\csc 2\phi\right), \tag{2.22}$$

$$\xi_n = \frac{k\pi\Gamma(1+\epsilon)}{1-\epsilon}\cot\phi\cos^2\phi\cos\tau_n - 2\Gamma\cot\phi\sin\tau_n. \tag{2.23}$$

Using (2.22) in the expressions for ξ_n, u_{n_x}, u_{n_y} gives

$$\begin{aligned}
\tau_n &= \arccos\left(\frac{k\pi(1-\epsilon)}{\Gamma(1+\epsilon)}\csc 2\phi\right),\\
\xi_n &= \frac{(k\pi\cot\phi)^2}{2} - \frac{2\cot\phi\sqrt{\Gamma^2(1+\epsilon)^2 - ((1-\epsilon)k\pi\csc 2\phi)^2}}{1+\epsilon},\\
u_{n_x} &= -k\pi\cot^2\phi,\\
u_{n_y} &= k\pi,
\end{aligned} \tag{2.24}$$

with $k = 1, 3, 5, \ldots$. The existence of these symmetric periodic orbits holds for more general driving functions $f(t)$. Namely, for any piecewise smooth function $f(t)$ which is periodic, there will be symmetric solutions of the form (2.24).

The stability of periodic orbits can be analyzed using the linearization of the map $\mathbf{J}$ (see Appendix A). Since the system is four-dimensional, the Jacobian of the map (2.18) is a 4×4 matrix,

$$\mathbf{J} = \begin{pmatrix}
\partial\tau_{n+1}/\partial\tau_n & \partial\tau_{n+1}/\partial\xi_n & \partial\tau_{n+1}/\partial u_{n_x} & \partial\tau_{n+1}/\partial u_{n_y}\\
\partial\xi_{n+1}/\partial\tau_n & \partial\xi_{n+1}/\partial\xi_n & \partial\xi_{n+1}/\partial u_{n_x} & \partial\xi_{n+1}/\partial u_{n_y}\\
\partial u_{n+1_x}/\partial\tau_n & \partial u_{n+1_x}/\partial\xi_n & \partial u_{n+1_x}/\partial u_{n_x} & \partial u_{n+1_x}/\partial u_{n_y}\\
\partial u_{n+1_y}/\partial\tau_n & \partial u_{n+1_y}/\partial\xi_n & \partial u_{n+1_y}/\partial u_{n_x} & \partial u_{n+1_y}/\partial u_{n_y}
\end{pmatrix}. \tag{2.25}$$

To evaluate the derivatives of τ_{n+1}, we write

$$\begin{aligned}
f(\tau_{n+1},\tau_n,\xi_n,u_{n_x},u_{n_y}) = -(\tau_{n+1}-\tau_n)^2 + \left(u_{n_y}\mp u_{n_x}\right)(\tau_{n+1}-\tau_n) + |\xi_n| \mp \xi_n\\
\mp 2m\Gamma\left(\sin\tau_n - \sin\tau_{n+1}\right) = 0,
\end{aligned} \tag{2.26}$$

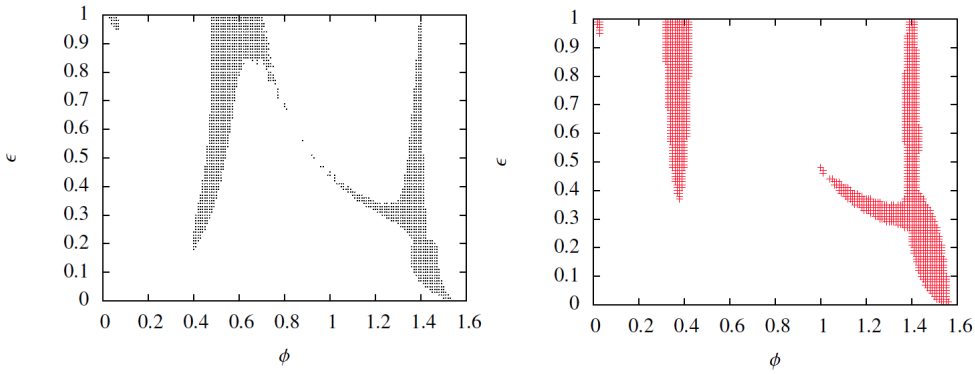

FIGURE 2.3: Stability regions of the symmetric fixed point solutions in (ϕ, ϵ) space for (a) $k = 1$; (b) $k = 3$. Here the wedge half-angle ϕ is plotted in radians.

and use the standard calculus identities to get (after evaluating the derivatives at the fixed point)

$$\begin{aligned}
\frac{\partial \tau_{n+1}}{\partial \tau_n} &= -\frac{\partial f/\partial \tau_n}{\partial f/\partial \tau_{n+1}} = \frac{1}{\epsilon}, & \frac{\partial \tau_{n+1}}{\partial \xi_n} &= -\frac{\partial f/\partial \xi_n}{\partial f/\partial \tau_{n+1}} = \frac{(1+\epsilon)\sin^2\phi}{k\pi\epsilon}, \\
\frac{\partial \tau_{n+1}}{\partial u_{n_x}} &= -\frac{\partial f/\partial u_{n_x}}{\partial f/\partial \tau_{n+1}} = -\frac{k\pi(1+\epsilon)\sin^2\phi}{2\epsilon}, & \frac{\partial \tau_{n+1}}{\partial u_{n_y}} &= -\frac{\partial f/\partial u_{n_y}}{\partial f/\partial \tau_{n+1}} = -\frac{k\pi(1+\epsilon)\sin^2\phi}{2\epsilon}.
\end{aligned} \tag{2.27}$$

The remaining derivatives, are computed using the chain rule; for example,

$$\frac{\partial \xi_{n+1}}{\partial \tau_n} = \left.\frac{\partial \xi_{n+1}}{\partial \tau_n}\right|_{\tau_{n+1}=\text{const.}} + \frac{\partial \xi_{n+1}}{\partial \tau_{n+1}}\frac{\partial \tau_{n+1}}{\partial \tau_n} = \frac{k\pi(1-\epsilon)}{\epsilon}. \tag{2.28}$$

The computation is straightforward, but tedious. Since we have a sequence of fixed points for $k = 1, 3, 5, \ldots$ the stability regions in the parameter space depend on the choice of k. In Fig. 2.3 we display the stability regions for a sample of k values in the (ϕ, ϵ)-parameter space. As we increase k, the energy of the fixed point orbit increases, which leads to smaller stability regions.

2.4 Numerical Results

2.4.1 Computing the Time of the Next Collision

Solving the time-of-collision equation

$$f(\tau_{n+1}) = -(\tau_{n+1}-\tau_n)^2+\left(u_{n_y} \mp u_{n_x}\right)(\tau_{n+1}-\tau_n)+|\xi_n|\mp\xi_n\mp 2\Gamma\cot\phi\,(\sin\tau_n-\sin\tau_{n+1}) = 0 \tag{2.29}$$

numerically for the smallest positive solution τ_{n+1} is non-trivial, since in a given interval there may be more than one positive root. Thus, applying a basic numerical root-finding procedure such as the bisection or Newton-Raphson method can lead to numerical errors when the bracketing interval fails to contain *exactly* one root, or (in the case of Newton-Raphson) when the initial guess converges to the wrong root. This feature is not unique to this system; in fact, such a phenomenon may be responsible for the appearance of "self-reanimating chaos," wherein analytically stable periodic orbits become unstable numerically, in sinusoidally driven Fermi Piston models [15].

In order to iterate the map (2.18) computationally, we need a numerical method which can safely compute the smallest positive root of (2.29). Our method is based on an algorithm developed by Hopkins and Miller in [29] in the study of the one-dimensional Fermi piston and gravitational bouncer models. This method relies on the fact that f can be written as the sum of quadratic and sinusoidal terms in τ_{n+1}, and therefore the roots of $\mathrm{d}^2 f/\mathrm{d}\tau_{n+1}^2$ can be computed analytically. This allows the isolation of the monotonic subintervals of f, ensuring that f possesses at most one root in these subintervals.

First, we note that one can easily place an upper bound on τ_{n+1}; namely, the time τ_{floor} at which the particle passes through $y(\tau_{\text{floor}}) = 0$. The time of the next collision must lie in the interval $I_n \equiv (\tau_n, \tau_{\text{floor}}]$. In order to avoid the problem of multiple roots, we require the subintervals of I_n, denoted by $S_n \equiv [\tau, \tau']$, on which $f(\tau_{n+1})$ is monotonic and for which either $f(\tau) \leq 0$ and $f(\tau') \geq 0$ or $f(\tau) \geq 0$ and $f(\tau') \leq 0$. If we can isolate the monotonic subintervals S_n of I_n, then in each S_n we are guaranteed *exactly* one root

of f. To find τ_{n+1} we need only find the root in the subinterval closest to τ_n. To find the monotonic intervals of I_n, we note that upon differentiating f twice with respect to τ_{n+1}, the resulting equation may be solved directly for the roots τ_* of $\mathrm{d}^2 f/\mathrm{d}\tau_{n+1}^2$:

$$\left.\frac{\mathrm{d}^2 f}{\mathrm{d}\tau_{n+1}}\right|_{\tau_{n+1}=\tau_*} = -2 \mp 2\Gamma \cot\phi \sin\tau_* = 0, \tag{2.30}$$

so that

$$\tau_* = \begin{cases} \arcsin\left(\mp\frac{1}{\Gamma\cot\phi}\right) \pm 2k\pi \\ \pi - \arcsin\left(\mp\frac{1}{\Gamma\cot\phi}\right) \pm 2\ell\pi \end{cases}, \tag{2.31}$$

where $k, \ell \in \mathbb{Z}$. The collection of these roots defines the intervals on which the derivative of f is monotonic. These monotonic subintervals of f' in $(\tau_n, \tau_{\text{floor}}]$, together with the roots of $f' = 0$, allow us to find the monotonic subintervals of f, and hence identify the smallest positive root as the root lying in the monotonic subinterval closest to τ_n, or, if we instead solve for the time interval $\Delta\tau_{n+1}$, the subinterval closest to zero.

We note that in principle this analysis could be extended to solving equations of the form

$$f(\tau) = p_n(\tau) + T(\tau) = 0, \tag{2.32}$$

where $p_n(\tau)$ is an n^{th} order polynomial and $T(\tau)$ is a continuous and n-times differentiable function which can be 'inverted', to solve for the roots of $f^{(n)}(\tau) = 0$.

2.4.2 Phase Space of the Elastic System

2.4.2.1 Small Oscillations - Elastic

First we examine the phase space for the elastic system, with small values of the oscillation strength $\Gamma \sim 0.01$ in order to see how the structures in the undriven wedge billiard's phase space survive small perturbations. In Fig. 2.4, we display several $2D$ projections of the phase space using the parallel and orthogonal components of the particle's velocity $(v_\parallel, v_\perp)$. Comparing these projections to the corresponding phase space

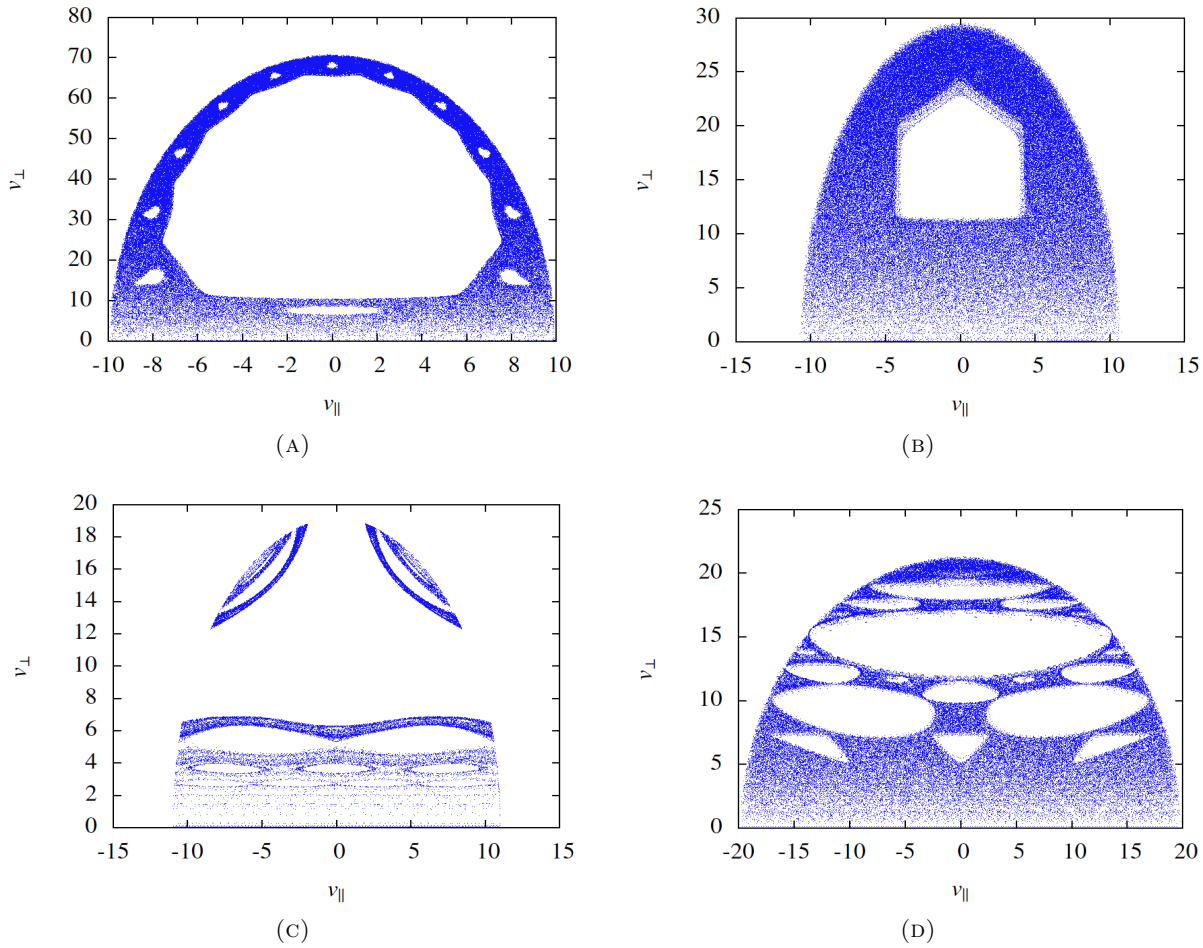

FIGURE 2.4: Projection of the phase space onto $(v_\parallel, v_\perp)$ for (A) $\phi = 10°$; (B) $\phi = 20°$; (C) $\phi = 30°$; and (D) $\phi = 43°$.

diagrams of the *static* wedge in [18, 19], we see that the general structures are indeed preserved under small perturbations. Above 45° the ergodicity of the system appears to be preserved as well.

2.4.2.2 Large Oscillations - Elastic

Increasing the oscillation strength Γ by an order of magnitude to ~ 0.1 is sufficient to destroy the structures found in the undriven wedge. For parameter values in this range, the generic behavior can be classified as either chaotic or stable in the form of periodic orbits and quasiperiodic islands surrounding these orbits. Two and three dimensional projections of these orbits no longer maintain the structure; hence, these plots do not offer significant qualitative information, and therefore are not included here.

As Γ is increased further to $\Gamma \sim 10$ and higher, we find that unbounded orbits in the form of *Fermi acceleration* arise, in addition to islands of stability and periodic orbits. This is in agreement with the so-called "LRA conjecture" [25–27] which states that a sufficient condition for Fermi acceleration in $2D$ smoothly driven billiards is the existence of a chaotic part in the phase space of the corresponding time-independent system.

2.4.3 Phase Space of the Inelastic System

Now we introduce energy loss due to collisions in the form of a coefficient of restitution $\epsilon < 1$. Naturally, for small values of either $\Gamma \lesssim 1$ or $\epsilon \lesssim 0.2$, the generic behavior of the particle is to fall near the vertex of wedge, completing a large number of small collisions. This behavior appears to be a two-dimensional version of the well-known phenomenon of *inelastic collapse* [16, 17] observed in one-dimensional gravitational bouncer models [13, 30]. Orbits which inelastically collapse complete an infinite number of collisions in a finite amount of time.

As we increase the oscillation strength, the energy loss in collisions is balanced by the energy gain due to the motion of the wedge. We find that for certain parameter values these competing mechanisms balance, allowing attracting orbits which do not experience inelastic collapse to emerge. In addition to the symmetric periodic orbits computed in 2.3, we find more general periodic orbits numerically, as well as what appears to be a chaotic attractor. We have computed the Lyapunov exponent σ (see Appendix A) for this attractor using the method of Wolf et al introduced in [31], and found $\sigma > 0$, which supports the chaotic nature of the orbit. In future work, we hope to explore this attractor in more detail e.g., compute the basin of attraction and investigate the bifurcation origins of the attractor.

Chapter 3

The Conic Billiard

3.1 The Model and the Mapping

In this part of the thesis we study a three-dimensional, *undriven* gravitational billiard. Namely, we are concerned with the motion of a uniformly accelerated particle in $\mathbb{R}^3$, colliding *elastically* with a linear cone of half-angle θ. In terms of the standard spherical co-ordinates[1] (r, θ, ϕ), the Lagrangian of a particle in the presence of a uniform gravitational field $\boldsymbol{g} = -g\hat{\boldsymbol{z}}$ is, in spherical co-ordinates,

$$\mathcal{L} = \frac{1}{2}\left(\dot{r}^2 + r^2\dot{\theta}^2 + r^2\sin^2\theta\dot{\phi}^2\right) - gr\cos\theta, \tag{3.1}$$

and the corresponding Hamiltonian (see Appendix A) is

$$H = \frac{1}{2}\left(p_r^2 + \frac{1}{r^2}\left(p_\theta^2 + \frac{p_\phi^2}{\sin^2\theta}\right)\right) + gr\cos\theta. \tag{3.2}$$

This governs the motion of the particle between collisions, which we assume to be elastic. Since between collisions the motion is purely integrable, there are (at least) 3 independent integrals of the motion restricting the particle to parabolic motion between

[1] We use θ to denote both the angle of the cone and the polar angle co-ordinate in spherical co-ordinates. Since a collision between the particle and boundary is equivalent to fixing θ (of the particle), the distinction between the two definitions of θ should be clear from context.

collisions; for example, the energy E, the z-component of angular momentum $\ell_z = xp_y - yp_x$, and p_x and p_y, the x and y components of the particle's linear momentum, are all conserved between collisions. During a collision, the energy as well as the linear and angular momenta are conserved. Hence there are two independent constants of the motion preserved by *both* the flow and the collision map,

$$I_1 = H = E, \qquad \text{and} \qquad I_2 = p_\phi = \ell_z, \tag{3.3}$$

which we identify as the energy and z-component of angular momentum, respectively. The presence of two conserved quantities reduces the dimension of the phase space of the system from six to four. Taking the natural Poincaré surface-of-section at the moment of collision (here $\rho = \sqrt{x^2 + y^2}$ is the cylindrical polar co-ordinate),

$$z = \rho \cot\theta = r\cos\theta \tag{3.4}$$

further reduces the dynamics to a three-dimensional map. In fact, as we shall show below, the azimuthal angle ϕ plays no role in the dynamics, and therefore the arbitrary initial condition $\phi = \phi_0$ is sufficient to describe all possible behavior of the system. Thus, a two-dimensional map characterizes the dynamics; in what follows we derive one such map. By a suitable transformation of the co-ordinates and time, the constants E and g can be re-scaled arbitrarily; for convenience, we choose units such that $E = g = \frac{1}{2}$, so that the three constants E, g, ℓ_z are consolidated into the single (dimensionless) parameter (where the factor of $\frac{1}{\sqrt{2}}$ is chosen for aesthetic purposes)

$$\ell' \equiv \frac{g\ell_z}{\sqrt{2}E^{3/2}}. \tag{3.5}$$

With this choice of units, energy and z-component of angular momentum conservation are expressed by (where we have replaced the momenta with the corresponding velocities)

$$1 = v_r^2 + v_\theta^2 + \frac{\ell'^2}{r^2\sin^2\theta} + r\cos\theta, \qquad \ell = (r\sin\theta)v_\phi. \tag{3.6}$$

The cone angle θ is restricted to $0^\circ \leqslant \theta \leqslant 90^\circ$. To bound the parameter ℓ', we re-write energy conservation as

$$\frac{\ell'^2}{r^2 \sin^2\theta} = 1 - v_r^2 - v_\theta^2 - r\cos\theta. \tag{3.7}$$

This implies that we have the following bound on $|\ell'|$ in terms of r,

$$|\ell'| \leqslant r\sin\theta\sqrt{1 - r\cos\theta} \tag{3.8}$$

or equivalently in terms of z,

$$|\ell'| \leqslant z\tan\theta\sqrt{1-z}. \tag{3.9}$$

On the other hand, energy conservation can also be written in terms of z,

$$1 = \boldsymbol{v}^2 + z. \tag{3.10}$$

Thus we must have $z \leqslant 1$, so that

$$z\tan\theta \leqslant \tan\theta \qquad \text{and} \qquad \sqrt{1-z} \leqslant 1, \tag{3.11}$$

and therefore

$$|\ell'| \leqslant \tan\theta. \tag{3.12}$$

In fact, it is easy to show that the function $f(z) = z\sqrt{1-z}$ has a maximum value of $\frac{2}{3\sqrt{3}}$ at $z = \frac{2}{3}$, and thus we can tighten our bound on ℓ':

$$|\ell'| \leqslant \frac{2\tan\theta}{3\sqrt{3}} \equiv \ell_{\max}. \tag{3.13}$$

By defining $\ell \equiv \ell'/\ell_{\max}$ we obtain a parameter which ranges from zero to one.

In between collisions the particle follows a parabolic trajectory; it follows from basic kinematics that the time interval $\tau_{n+1} \equiv t_{n+1} - t_n$ is given by the smallest positive root

of the cubic equation

$$\tau_{n+1}^3 - 8v_{n_z}\tau_{n+1}^2 + 16\left[v_{n_z}^2 - \cot^2\theta(v_{n_x}^2 + v_{n_y}^2) - \frac{\cot\theta}{2}\sqrt{x_n^2+y_n^2}\right]\tau_{n+1} + 32\left[v_{n_z}\cot\theta\sqrt{x_n^2+y_n^2} - \cot^2\theta\left(x_n v_{n_x} + y_n v_{n_y}\right)\right] = 0, \quad (3.14)$$

which is equivalent to

$$\tau_{n+1}^3 + 8(v_{n_\theta}\sin\theta - v_{n_r}\cos\theta)\tau_{n+1}^2 + 16\left[v_{n_\theta}^2 - \cot\theta\left(\cot\theta(v_{n_\theta}^2 + v_{n_\phi}^2) + 2v_{n_r}v_{n_\theta}\right) - \frac{r_n\cos\theta}{2}\right]\tau_{n+1} - 32r\,v_{n_\theta}\cot\theta = 0 \quad (3.15)$$

in spherical coordinates. Geometrically, we are solving for the intersection of a parabola and a hyperbola. Hence this cubic equation will have three real roots (the fourth root of the intersection is just $\tau_{n+1} = 0$ i.e., the intersection of the n^{th} collision). The roots of this cubic equation are long and complicated, and do not yield any physical insight; thus, they are not included here. To analyze the effects of a collision, spherical co-ordinates are natural for this system. This is because the equations relating pre– and post–collision components of the billiard's velocity become especially simple in these co-ordinates (note that $\hat{\boldsymbol{\theta}}$ is orthogonal to the surface of the cone, and $\hat{\boldsymbol{r}}, \hat{\boldsymbol{\phi}}$ are parallel to it). If $v_{n+1_i}^-$ denotes the i^{th} component of the particle's velocity just *before* the $n+1^{\text{st}}$ collision, and $v_{n+1_i}^+$ the corresponding component just *after* the $n+1^{\text{st}}$ collision, then the vector equation (here $\boldsymbol{n} = \hat{\boldsymbol{\theta}}$ is a unit normal to the surface of the cone)

$$\boldsymbol{v}^+ = \boldsymbol{v}^- - 2(\boldsymbol{v}\cdot\boldsymbol{n})\boldsymbol{n} \quad (3.16)$$

is equivalent to the three component equations

$$v_{n+1_r}^+ = v_{n+1_r}^-, \qquad v_{n+1_\phi}^+ = v_{n+1_\phi}^-, \qquad v_{n+1_\theta}^+ = -v_{n+1_\theta}^-. \quad (3.17)$$

Thus far, we have eliminated two degrees of freedom using constants of the motion. This suggests that a three-dimensional surface-of-section is required to capture the dynamics. However, it turns out that *two* variables, r and v_r, are sufficient to determine the subsequent motion of the particle. To see this, suppose that we know the value of these two quantities after the n^{th} collision, r_n and v_{n_r}. Then we immediately know the value of θ, since at each collision this is just the polar angle of the cone; additionally, we know the ϕ-component of the particle's velocity:

$$v_{n_\phi} = \frac{\ell}{r_n \sin\theta}. \tag{3.18}$$

Using this in the energy conservation expression permits us to solve for $v_{n_\theta}^2$ in terms of r_n and v_{n_r}:

$$v_{n_\theta}^2 = 1 - r_n \cos\theta - v_{n_r}^2 - \frac{\ell^2}{r_n^2 \sin^2\theta}. \tag{3.19}$$

Although it seems we may only know v_{n_θ} up to a sign, in fact we are safe to choose the *negative* root, since v_θ is the component of the velocity orthogonal to the surface of the cone in the direction of $\hat{\boldsymbol{\theta}}$, which, due to the convention $\hat{\boldsymbol{\theta}} \equiv \hat{\boldsymbol{\phi}} \times \hat{\boldsymbol{r}}$, cannot be *positive* after a collision. Moreover, as we shall see below, the azimuthal angle ϕ plays no role in the dynamics; thus, it can be fixed arbitrarily at $t = 0$ and subsequently eliminated from the mapping, as only the *difference* in ϕ appears in the equations (and this quantity can be computed purely in terms of r, v_r and the time of the next collision). Thus, to complete the mapping we need only compute the time interval from (3.15), $r_{n+1} = \csc\theta\sqrt{x_{n+1}^2 + y_{n+1}^2}$ and v_{n+1_r} from (see Appendix B)

$$\begin{aligned} v_{n+1_r} = v_{n_r}(\sin^2\theta\cos\varphi_{n+1} + \cos^2\theta) + v_{n_\theta}\sin\theta\cos\theta(\cos\varphi_{n+1} - 1) \\ + v_{n_\phi}\sin\varphi_{n+1}\sin\theta - \frac{1}{2}\tau_{n+1}\cos\theta, \end{aligned} \tag{3.20}$$

where $\varphi_{n+1} \equiv \phi_{n+1} - \phi_n$ is the difference in azimuthal angle between collisions, given by

$$\varphi_{n+1} = \arctan\left(\frac{v_{n_\phi}\tau_{n+1}}{r_n\sin\theta + (v_{n_r}\sin\theta + v_{n_\theta}\cos\theta)\tau_{n+1}}\right), \tag{3.21}$$

with care being taken to choose the correct quadrant in the xy-plane. In terms of these quantities the mapping is

$$r_{n+1}^2 = \left((v_{n_r} + v_{n_\theta} \cot\theta)^2 + \frac{\ell^2}{r_n^2} \right) \tau_{n+1}^2 + 2r_n \left(v_{n_r} + v_{n_\theta} \cot\theta \right) \tau_{n+1} + r_n^2, \tag{3.22}$$

$$v_{n+1_r} = v_{n_r} \left(\sin^2\theta \cos\varphi_{n+1} + \cos^2\theta \right) + v_{n_\theta} \sin\theta \cos\theta \left(\cos\varphi_{n+1} - 1 \right) + v_{n_\phi} \sin\theta \sin\varphi_{n+1} - \frac{1}{2}\tau_{n+1} \cos\theta. \tag{3.23}$$

By utilizing some trigonometric identities, it may be shown that (see Appendix B)

$$\sin\varphi_{n+1} = \frac{v_{n_\phi} \tau_{n+1}}{r_{n+1} \sin\theta}, \tag{3.24}$$

and

$$\cos\varphi_{n+1} = \frac{r_n + (v_{n_r} + v_\theta \cot\theta)\tau_{n+1}}{r_{n+1}}. \tag{3.25}$$

After defining the convenient reduced variables $\rho \equiv r\sin\theta$, $u_r \equiv v_r \sin\theta, u_\theta \equiv v_\theta \cos\theta$, the mapping can be rewritten as

$$\rho_{n+1}^2 = \left[(u_{n_r} + u_{n_\theta})^2 + \frac{\ell^2}{\rho_n^2} \right] \tau_{n+1}^2 + 2\rho_n \left(u_{n_r} + u_{n_\theta} \right) \tau_{n+1} + \rho_n^2, \tag{3.26}$$

$$u_{n+1_r} = \frac{\sin^2\theta}{\rho_{n+1}} \left\{ \left[(u_{n_r} + u_{n_\theta})^2 + \frac{\ell^2}{\rho_n^2} \right] \tau_{n+1} + \rho_n \left(u_{n_r} + u_{n_\theta} \right) \right\} + u_{n_r} \cos^2\theta - u_{n_\theta} \sin^2\theta - \frac{1}{4}\tau_{n+1} \sin 2\theta. \tag{3.27}$$

Of course, our 'reduced variable' ρ is just the cylindrical polar co-ordinate; however, u_r is not the corresponding velocity component v_ρ. In fact, $v_\rho = u_r + u_\theta$. Although this suggests that the conjugate variables (ρ, v_ρ) should be used for the mapping, these two variables are *insufficient* to determine the subsequent trajectory of the particle. Writing

energy conservation in terms of cylindrical polar co-ordinates, we see that

$$1 = v_\rho^2 + v_z^2 + \frac{\ell^2}{\rho^2} + \rho \cot\theta. \tag{3.28}$$

Thus, if we know ρ and v_ρ, then the square of v_z is given by

$$v_z^2 = 1 - v_\rho^2 - \frac{\ell^2}{\rho^2} - \rho \cot\theta. \tag{3.29}$$

However, without some additional piece of information regarding the sign of v_z, a priori we have no way of determining which square root to take. Thus, (r, v_r) or equivalently (ρ, u_r) seem to be the co-ordinates of choice for the conic billiard.

Although in principle we can eliminate v_θ or u_θ from the mapping via energy conservation, the equations become considerably more complicated and yield little additional insight. Moreover, we find that computing periodic orbits of the system is easier when using this 'implicit' form of the mapping.

The reason we choose (r, v_r) as our primary mapping variables is simple: they are area-preserving i.e., the determinant of the Jacobian matrix $\mathbf{J}$ is equal to unity (see Appendix A). Another sensible choice would be $(\mathrm{sgn}(v_r)v_\parallel, v_\perp)$, where $v_\parallel$ and $v_\perp$ are the normal and tangential components of the velocity with respect to the cone boundary. Although these variables are sufficient to fully determine the dynamics, they are not area-preserving. In the next section, we shall utilize several times the area-preserving nature of (r, v_r) in the computation of stability eigenvalues. In deriving specific fixed points and periodic orbits, however, the reduced mapping (3.26)-(3.27) is more suitable. Since the variables are not area-preserving, however, they are not ideal for surface-of-section plots.

3.2 Simple Properties of the Mapping

First we examine some general properties of the mapping. If $\ell = 0$ the conic system reduces to the two-dimensional wedge system, so that the Hamiltonian becomes

$$H_{\text{wedge}} = \frac{1}{2}\left(p_r^2 + \frac{p_\theta^2}{r^2}\right) + r\cos\theta. \tag{3.30}$$

Hence, for $\ell = 0$ the cone becomes integrable for three cases: (i) $\theta \to 0°$, (ii) $\theta = 45°$, and (iii) $\theta \to 90°$. In the first case, the potential becomes purely radial in the limit i.e.,

$$H \to \frac{1}{2}\left(p_r^2 + \frac{p_\theta^2}{r^2}\right) + r, \tag{3.31}$$

implying the conservation of $p_\theta = r^2\dot{\theta}$, which is also preserved by the collision map. For $\theta = 45°$, co-ordinates parallel and orthogonal to the wedge surface can be defined so that the motion becomes separable. Finally, for $\theta = 90°$ the motion becomes simply that of a projectile bounded from below by a horizontal floor. In this case, the motion is unbounded.

For $\ell \neq 0$, we lose integrability at $\theta = 45°$. However, we retain the integrable limit $\theta \to 90°$, as the above argument is unaffected by the introduction of a nonzero z-component of angular momentum. Additionally, the limit $\theta \to 0°$ remains integrable as long as we simultaneously take $\ell \to \ell_{\max}$. Examining the Hamiltonian

$$H = \frac{1}{2}\left(p_r^2 + \frac{p_\theta^2}{r^2}\right) + \frac{\ell^2}{r^2\sin^2\theta} + r\cos\theta, \tag{3.32}$$

we see that if we naively take the limit $\theta \to 0$ the term proportional to $\sin^{-2}\theta$ diverges. However, if we instead take $\theta \to 0$ with $\ell \to \ell_{\max} \sim \tan\theta$, we see that

$$H \to \frac{1}{2}\left(p_r^2 + \frac{p_\theta^2}{r^2}\right) + \frac{a}{r^2} + r, \tag{3.33}$$

where $a = \frac{4}{27}$ is a constant. Hence the potential again becomes indistinguishable from

a central potential in this limit, implying that the quantity p_θ is conserved, and the motion integrable.

3.3 Periodic Orbits

Imposing the conditions $\rho_{n+1} = \rho_n = \rho$, $u_{n+1_r} = u_{n_r} = u_r$ on the mapping, we arrive at

$$0 = \left[(u_r + u_\theta)^2 + \frac{\ell^2}{\rho^2}\right]\tau + 2\rho(u_r + u_\theta), \tag{3.34}$$

$$u_r = \frac{\sin^2\theta}{\rho}\left\{\left[(u_r + u_\theta)^2 + \frac{\ell^2}{\rho^2}\right]\tau + \rho(u_r + u_\theta)\right\} + u_r\cos^2\theta - u_\theta\sin^2\theta - \frac{\tau}{4}\sin 2\theta. \tag{3.35}$$

The first equation is equivalent to

$$\tau = \frac{-2\rho(u_r + u_\theta)}{(u_r + u_\theta)^2 + \ell^2/\rho^2}. \tag{3.36}$$

Evidently this holds for all fixed points of the map. Using this in the mapping equations for u_{n+1_r} and u_{n+1_θ} gives

$$\tau = -4\tan\theta(u_r + u_\theta) \tag{3.37}$$

for u_{n+1_r}, and

$$\tau = -4\cot\theta\, u_r - 4\tan\theta\, u_\theta \tag{3.38}$$

for u_{n+1_θ}. Thus either $u_r = 0$ or $\theta = \frac{\pi}{4}$. In the case $u_r = 0$, setting the two expressions for τ equal gives

$$\rho = 2\tan\theta\left(u_\theta^2 + \frac{\ell^2}{\rho^2}\right). \tag{3.39}$$

If $\ell = 0$, then it is easily verified that

$$\rho = \frac{\sin 2\theta}{2 + \cos 2\theta}, \qquad u_r = 0 \tag{3.40}$$

is a fixed point. In the case that $u_r = 0$, we can apply energy conservation to arrive at

$$u_\theta^2 = \frac{\cos^2\theta(\rho^2 - 3\ell^2)}{\rho^2(2+\cos 2\theta)}. \tag{3.41}$$

Back substitution for ρ results in

$$\frac{2\cos^2\theta}{2+\cos 2\theta} = \rho\cot\theta - \frac{2\ell^2\sin^2\theta}{\rho^2(2+\cos 2\theta)}, \tag{3.42}$$

which is equivalent to the cubic equation

$$(2+\cos 2\theta)\cot\theta\,\rho^3 - 2\cos^2\theta\,\rho^2 - 2\ell^2\sin^2\theta = 0. \tag{3.43}$$

Clearly, if we set $\ell = 0$ in the above equations we recover the limiting case found above. Although the equation determining ρ is cubic, it turns out that for all parameter values there is only one real root of this equation. Hence there is a single fixed point

$$\rho = \rho_*, \qquad u_r = 0, \qquad \text{where } \rho_* \text{ solves (3.43)}. \tag{3.44}$$

The stability of this orbit can be analyzed in terms of the eigenvalues of the Jacobian matrix. As is shown in Appendix A, the stability condition that the eigenvalues of the Jacobian are less than one in modulus is equivalent to, for an area-preserving map, the condition

$$|\mathrm{Tr}\,\mathbf{J}| < 2. \tag{3.45}$$

Of course, since the (ρ, u_r) map is not area-preserving, we must instead use the Jacobian of the (r, v_r) map. In terms of these variables the fixed point is

$$r = r_*, \qquad v_r = 0, \tag{3.46}$$

where r_* is given by

$$(2+\cos 2\theta)\cos\theta r_*^3 - 2\cos^2\theta r_*^2 - 2\ell^2 = 0. \tag{3.47}$$

Since the mapping depends *explicitly* on the time between collisions τ_{n+1}, in computing the necessary derivatives we must take care to use the chain rule i.e.,

$$\frac{\partial r_{n+1}}{\partial r_n} = \frac{\partial r_{n+1}}{\partial r_n}\bigg|_{\tau_{n+1}=\text{const.}} + \frac{\partial r_{n+1}}{\partial \tau_{n+1}}\frac{\partial \tau_{n+1}}{\partial r_n}, \qquad \frac{\partial v_{n+1_r}}{\partial v_{n_r}} = \frac{\partial v_{n+1_r}}{\partial v_{n_r}}\bigg|_{\tau_{n+1}=\text{const.}} + \frac{\partial v_{n+1_r}}{\partial \tau_{n+1}}\frac{\partial \tau_{n+1}}{\partial v_{n_r}}, \tag{3.48}$$

where the derivatives of τ_{n+1} are computed using implicit differentiation on the cubic equation for the time interval i.e., for example,

$$\frac{\partial \tau_{n+1}}{\partial r_n} = -\frac{\partial f/\partial r_n}{\partial f/\partial \tau_{n+1}}, \tag{3.49}$$

where $f(\tau_{n+1}, r_n, v_{n_r}) = 0$ is defined by (3.15). The explicit expression of $\operatorname{Tr}\mathbf{J}$ is long and complicated, and is not shown here. Instead, we will state that these solutions are in general stable, or *elliptic*, for $\ell \neq 0$, as well as $\ell = 0$ for $0 \leqslant \theta \leqslant 45°$. For $\ell = 0$ and $\theta > 45°$, these solutions become unstable, or *hyperbolic*.

For more general periodic orbits, we note that for $\ell = 0$ there are, for example, well-known period-m orbits of the form

$$\rho = \tan\theta\left(1 - \frac{m^2\cos^2\theta + \sin^2\theta}{1-(m+1)^2\cos^2\theta\cos 2\theta}\right), \qquad u_r = \frac{m\sin\theta\cos\theta}{\sqrt{1-(m+1)^2\cos^2\theta\cos 2\theta}}. \tag{3.50}$$

Such solutions clearly hold for the conic billiard when $\ell = 0$; however, generalizing these solutions to $\ell \neq 0$ is difficult to do analytically, due to the implicit nature of the mapping. However, higher order periodic orbits can be found numerically.

3.4 Numerical Results

3.4.1 Wedge-like behavior: small ℓ

For small values of ℓ, which corresponds to small values of v_ϕ, the phase space is qualitatively similar to that of the wedge billiard. That is, for $0 \leqslant \theta \lesssim 45°$ the system is in general *mixed*, consisting of regular and chaotic regions coexisting in the phase space. However, at the special values $\theta = 0°, 45°$, and $90°$ the system is integrable for $\ell = 0$.

In Fig. 3.1 we display the Poincaré surface-of-section (r_n, v_{n_r}) for a variety of cone angles at $\ell = 0.1$. We note that the general structure of the phase space is quite typical of two-dimensional area-preserving mappings; we see coexisting chaotic and regular regions in the phase space.

As θ is varied, we see a number of interesting bifurcation processes as periodic orbits lose and gain stability. The behavior is qualitatively similar to that of the wedge, as the phase space is mixed for $0 \leqslant \theta \leqslant \theta_*$ and ergodic for $\theta > \theta_*$, where $\theta_* = 45°$ for the wedge and is dependent on ℓ for $0 < \ell \lesssim 0.1$.

3.4.2 Large-ℓ values

As ℓ is increased, the relative amount of chaos in the phase space becomes smaller. As we increase the allowable v_ϕ, we lose the "wedge-like" behavior and the dynamics become more regular. In Fig. 3.2 we plot the Poincaré surface-of-section (r_n, v_{n_r}) for $\ell = 0.5$ and a variety of θ values. The value $\ell = 0.5$ is representative of the range $0.1 < \ell \lesssim 0.7$. As $\ell > 0.7$ the behavior approaches the integrable limit $\ell \to 1$, with the amount of chaos decreasing (and disappearing completely in the limit).

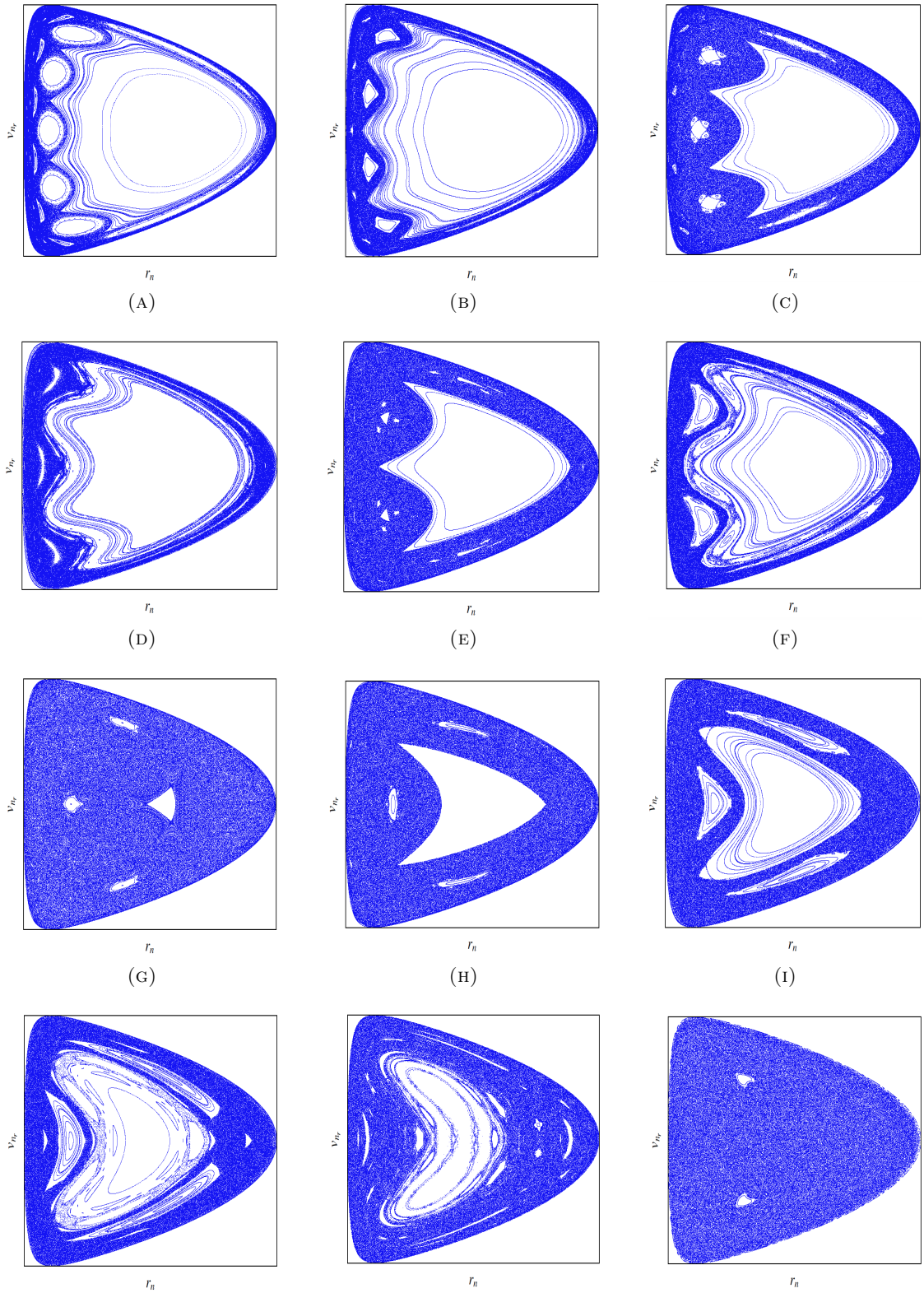

FIGURE 3.1: SOS at $\ell = 0.1$ for (A) $\theta = 15°$; (B) $\theta = 18.5°$; (C) $\theta = 21°$; (D) $\theta = 24.5°$; (E) $\theta = 27°$; (F) $\theta = 30.5°$; (G) $\theta = 34°$; (H) $\theta = 37.5°$; (I) $\theta = 41°$; and (J) $\theta = 44.5°$; (K) $\theta = 47°$; (L) $\theta = 50.5°$. For larger θ the system appears ergodic.

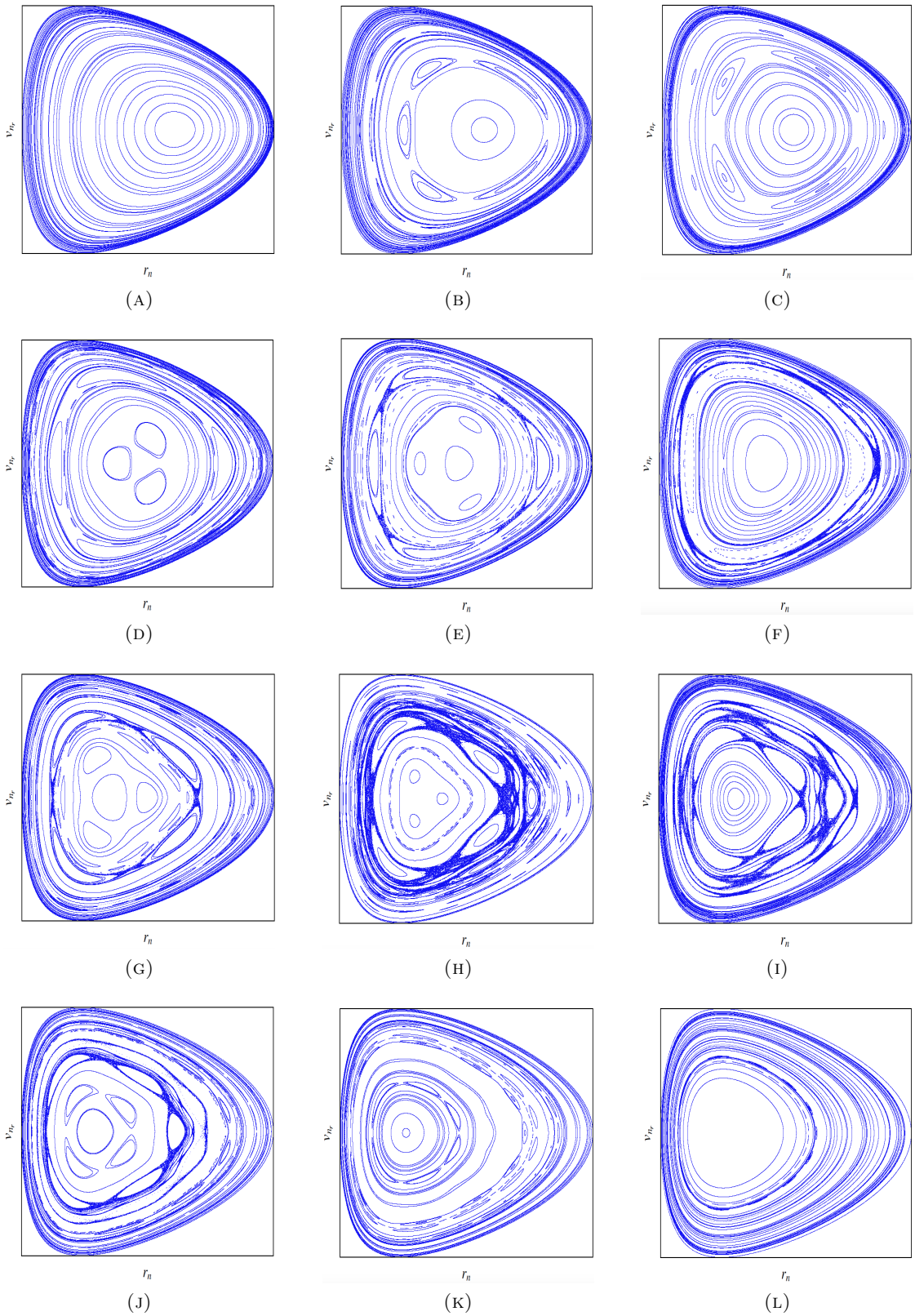

FIGURE 3.2: SOS at $\ell = 0.5$ for (A) $\theta = 10°$; (B) $\theta = 25.5°$; (C) $\theta = 34°$; (D) $\theta = 42°$; (E) $\theta = 44°$; (F) $\theta = 50°$; (G) $\theta = 60°$; (H) $\theta = 63.5°$; (I) $\theta = 67°$; (J) $\theta = 70.5°$; (K) $\theta = 77°$; (L) $\theta = 81.5°$.

Chapter 4

Conclusion

Gravitational billiard systems are simple, experimentally accessible models exhibiting the fundamental aspects common to nonlinear and chaotic systems. The parabolic motion of the particle between collisions makes the integration of differential equations unnecessary, and the geometry of trajectories easily visualized. In two dimensions, the most widely studied such system is the wedge billiard. In this work, the nonlinear dynamics of two distinct generalizations of this system have been investigated. First, we introduced a driven and dissipative version of the wedge, and derived a four-dimensional discrete map describing the dynamics. In contrast to previous work done on the driven wedge, we used an event-driven model which neglects rotational effects in order to avoid needing to numerically integrate the differential equation governing the flight of the billiard. This allowed further analytical work to be done, included the computation of fixed points of the map. We investigated the linear stability of these fixed points analytically and computed the stability regions in the parameter space numerically. Next, we explored the phase space of the system for various values of the parameters. We found that for weak driving and elastic collisions, the structures of the static wedge survived perturbations. As the strength of the driving was increased, unbounded orbits i.e., Fermi acceleration was observed. We then studied the inelastic system i.e., $\epsilon < 1$. The presence of energy loss due to collisions leads to a dramatic change in behavior.

Namely, we found that the existence of periodic and chaotic attracting orbits required a dynamical balance between the energy lost in collisions and the energy gained due to the wedge boundary's motion. This amounts to requiring the driving strength parameter Γ to be large enough to overcome the restitution coefficient ϵ. If this balance was upset, a two-dimensional version of inelastic collapse was observed, where the particle completed a large number of collisions near the wedge vertex.

In the second part of this work, we introduced a three-dimensional gravitational billiard, called the conic billiard, consisting of a particle falling in a linear cone. We reduced this system to a two-dimensional area-preserving discrete map with two parameters. We found several integrable limits of the system, and computed fixed points of the map and examined their linear stability. Next, we investigated the phase space of the conic billiard in terms of the two parameters, θ and ℓ. For small ℓ values, we found the system's phase space was qualitatively similar to that of the wedge, with a mixed phase space for $0^\circ < \theta < \theta_*$ and apparent ergodicity for $\theta > \theta_*$, where θ_* was an angle dependent on the value of ℓ. As we increased ℓ, we found the departure from the wedge billiard to be dramatic. Namely, the relative amount of chaos in the phase space became smaller as ℓ was increased, and the periodic orbits and KAM islands dominate the structure of the phase space.

In future work on the driven wedge billiard, we would like to investigate the structure and bifurcation origins of the chaotic attractor we found in the inelastic case. In future work on the conic billiard, we would like to include rotational effects, as well as examine driven versions of this system. One possible way to introduce time-dependence to the conic billiard would be to 'spin' the cone sinusoidally. This would have the advantage that only the collision equations would need modification; computing the time of the next collision which, as we have seen, is in general a non-trivial numerical task, would be no more difficult than in the undriven conic system studied here.

Appendix A

Review of Nonlinear Dynamics

Introduction

Inspired by the qualitative theory of ordinary differential equations, dynamical systems theory involves the study of processes changing in time. We describe such processes in terms of differential equations or iterative maps. For *nonlinear* systems, the equations governing the dynamics are in general hard[1] to solve analytically. Thus, in *nonlinear dynamics* we focus on the qualitative behavior of systems, rather than the quantitative aspects of a single trajectory. In this appendix, we recapitulate some basic definitions and tools often used in nonlinear dynamics. For a more detailed introduction to the field, cf. for example [32].

Definitions

Three components constitute a dynamical system: (i) a phase, or state space $\mathcal{M}$ whose points $\boldsymbol{x}$ describe the different possible states of the system; (ii) time t (in either continuous or discrete steps); and (iii) an evolution rule $\boldsymbol{F}(\boldsymbol{x}, t)$, which describes the fate

[1] read: impossible

of an initial state $\boldsymbol{x}_0$ at a time t later by $\boldsymbol{F}(\boldsymbol{x}_0, t)$. The evolution rule is a map

$$\boldsymbol{F} : \mathcal{M} \to \mathcal{M}, \tag{A.1}$$

and the infinite time-trajectory of an initial point $\boldsymbol{x}_0$ is called the *orbit* of $\boldsymbol{x}_0$. For continuous systems orbits are smooth curves, and for discrete maps sequences of points. For a generic (nonlinear) dynamical system, we can classify all orbits as either periodic i.e., $\boldsymbol{F}(\boldsymbol{x}, t) = \boldsymbol{F}(\boldsymbol{x}, t+p)$ for some p, or aperiodic $\boldsymbol{F}(\boldsymbol{x}, t) \neq \boldsymbol{F}(\boldsymbol{x}, t')$ for all $t \neq t'$. However, while periodic behavior is the simplest example of an orbit preserved by the dynamics, more general invariant *manifolds*, such as the invariant tori of Hamiltonian systems, can be preserved as well. In such systems, periodic motion is considered along with quasiperiodic orbits[2] as belonging to the class of *regular* orbits. In addition to regular orbits, there exist aperiodic orbits for which the asymptotic dynamics are sufficiently complicated to appear stochastic; this behavior, called *chaos*, is made slightly more precise by stating that nearby orbits diverge exponentially in time i.e., the phase space distance $\delta\boldsymbol{x}(t) \equiv \boldsymbol{x}_0(t) - \boldsymbol{x}(t)$ between two orbits which have nearby initial conditions satisfies

$$\|\delta\boldsymbol{x}(t)\| \simeq \mathrm{e}^{\sigma t}\|\delta\boldsymbol{x}(0)\|, \tag{A.2}$$

where $\sigma > 0$ for chaotic systems.[3] Such behavior immediately renders the prediction of an individual trajectory difficult; thus, instead of focusing on precise predictions we hope to describe the qualitative behavior of systems in terms of collections of initial conditions. This amounts to understanding the geometry of the phase space, and it turns out that although in general almost all orbits of a generic system are aperiodic, the relatively rare periodic orbits play an integral role in investigating its *qualitative* features, as well as partitioning the phase space in a way which is invariant under the dynamics. Thus, the basic strategy when presented with a nonlinear system is as follows:

[2] A quasiperiodic orbit is one confined to the surface of a torus in the state space.

[3] More precisely, in addition to the exponential divergence of nearby trajectories we require that orbits are not unbounded i.e., the dynamics is confined to some finite region of phase space. While there is no universal definition of chaos, it is (roughly) characterized by two properties: *local* instability and *global* (topological) mixing.

- First, we represent the system with a state $\boldsymbol{x} \in \mathcal{M}$ in an n-dimensional state space $\mathcal{M}$ whose evolution is given in terms of either a set of differential equations

$$\frac{\mathrm{d}\boldsymbol{x}}{\mathrm{d}t} = \boldsymbol{F}(\boldsymbol{x}, t, \boldsymbol{\mu}), \tag{A.3}$$

  or a set of discrete maps

$$\boldsymbol{x}_{n+1} = \boldsymbol{F}(\boldsymbol{x}_n, t, \boldsymbol{\mu}), \tag{A.4}$$

  where $\boldsymbol{\mu} \in \mathbb{R}^\ell$ are the ℓ parameters of the system.[4]

- Investigate the simplest possible orbits of the system; usually these take the form of *fixed points* or *equilibria*, as well as higher order periodic orbits.

- Analyze the stability of these orbits by linearizing the dynamics; this involves the magnitudes of the eigenvalues of the Jacobian matrix $\mathbf{J}$ of the system.

- Examine possible bifurcations of periodic orbits as the parameters of the system are varied, as well as the influence of such orbits on nearby initial conditions (e.g., basins of attraction).

- Numerically investigate the global aspects of the phase space, quantifying chaotic behavior using the leading Lyapunov exponent of the system.

In the rest of this appendix we define more precisely the tools we utilize in implementing the above strategy.

Poincaré surface-of-section

Any continuous–time dynamical system can be replaced by a discrete–time one by slicing the state space at a prescribed event. This event could be the orbit crossing some hypersurface in $\mathcal{M}$ (commonly the *energy* hypersurface in conservative systems), or one of the coordinates meeting a certain condition (as in the intersection of a particle

[4] For the systems considered in this work, we find that discrete-time dynamics are natural; we replace the continuous flow with a discrete map by choosing a suitable Poincaré surface-of-section.

with some boundary). A *Poincaré surface-of-section* (SOS) reduces the dimensionality of the system by one without information being lost; given a set of SOS points and the mapping(s) connecting them, the full flow can always be recovered. In fact, the dynamics "transverse" to the flow at a SOS is critical to understanding the stability (i.e., attracting or repelling nearby orbits) of the flow; it turns out that the induced *Poincaré map* $\mathcal{P} : \tilde{\boldsymbol{x}} \to \tilde{\boldsymbol{x}}'$ which maps a point $\tilde{\boldsymbol{x}}$ on the $(n-1)$–dimensional hypersurface to a successive point $\tilde{\boldsymbol{x}}'$ on the same surface suffices to understand the nature of the flow.

Equilibria/Fixed Points

In understanding any dynamical system, a reasonable first step is to ask: are there orbits which are *invariant* (in the sense that the orbit as a whole remains unchanged under time-translation of the system) under the flow or map? This leads directly to a search for *fixed* and *periodic* orbits as the simplest possible behavior of the system. First, we consider a fixed point or equilibrium solution, defined as a point $\boldsymbol{x}_0 \in \mathcal{M}$ such that $\boldsymbol{F}(\boldsymbol{x}_0, t) = \boldsymbol{x}_0$ for all time t. By Taylor expanding an infinitesimally displaced orbit $\boldsymbol{x} + \delta\boldsymbol{x}$ to first order, we find that for an n-dimensional continuous system of the form (A.3), we have

$$F_i(\boldsymbol{x}_0 + \delta\boldsymbol{x}) \simeq F_i(\boldsymbol{x}_0) + \sum_{j=1}^{n} \left.\frac{\partial F_i}{\partial x_j}\right|_{\boldsymbol{x}=\boldsymbol{x}_0} + \cdots \tag{A.5}$$

so that the evolution of the perturbed orbit is governed by[5]

$$\delta\boldsymbol{x}(t) = \frac{\partial \boldsymbol{x}(t)}{\partial \boldsymbol{x}_0(0)} \cdot \delta\boldsymbol{x}_0 \equiv \mathbf{J}(t) \cdot \delta\boldsymbol{x}_0, \tag{A.6}$$

where $\mathbf{J}(t)$ is the Jacobian matrix[6] with entries $\mathsf{J}_{ij}(t) = \partial x_i(t)/\partial x_j(0)$. For a discrete system of the form (A.4), the corresponding result is

$$\delta\boldsymbol{x}_{n+1} = \mathbf{J} \cdot \delta\boldsymbol{x}_n \tag{A.7}$$

[5] Note: this equation describes the dynamics in the tangent space of $\mathcal{M}$.
[6] Other commonly used notations for the Jacobian are $D\boldsymbol{F}$ and $\mathrm{d}\boldsymbol{F}$.

with the Jacobian matrix defined as

$$\mathbf{J} \equiv \frac{\partial \boldsymbol{x}_{n+1}}{\partial \boldsymbol{x}_n} = \frac{\partial \boldsymbol{F}}{\partial \boldsymbol{x}_n}. \tag{A.8}$$

The eigenvalues and eigenvectors of the Jacobian describe the behavior of orbits near the fixed point in the following fashion:[7] if $\{\Lambda_i\}$ denotes the set of eigenvalues with corresponding eigenvectors $\{\boldsymbol{e}_i\}$, we say that a fixed point $\boldsymbol{x}_0$ is

1. *elliptic* or *stable*, if $|\Lambda_i| < 1$ for all i;
2. *unstable* or *repelling*, if $|\Lambda_i| > 1$ for all i;
3. *hyperbolic* or *semi-stable*, if $|\Lambda_i| < 1$ for some i and $|\Lambda_j| > 1$ for some j; and
4. *marginal* , if $|\Lambda| = 1$ for all i.

The eigenvalues of the Jacobian matrix describe the stretching ($|\Lambda_j| > 1$) and compressing ($|\Lambda_j| < 1$) of a ball of points surrounding a fixed point in a finite time.

The stability of a period-ℓ orbit is determined by the eigenvalues of the *total* Jacobian matrix, which is given by (the multiplicative structure of Jacobian matrices follows from the chain rule of functional composition)

$$\mathbf{J}^{\ell}(\boldsymbol{x}_0) = \mathbf{J}(\boldsymbol{x}_{\ell-1}) \cdots \mathbf{J}(\boldsymbol{x}_1) \cdot \mathbf{J}(\boldsymbol{x}_0). \tag{A.9}$$

Quantifying Chaos – the Leading Lyapunov exponent

If all points in a neighborhood converge to a single orbit, the "attractor" is either a fixed point or a periodic orbit. For these orbits, motion is predictable in the sense that small changes to initial conditions result in only slightly different motion. However, for certain nonlinear systems we find attractors for which the motion is unpredictable in

[7] Here we state the conditions for a discrete map (A.4); the corresponding conditions for continuous systems are similar, but not used in this work, and thus not included.

the sense that nearby orbits *diverge* in time, and result in wildly different asymptotic dynamics. For these "strange attractors," the motion is chaotic, and characterized by *sensitive dependence on initial conditions*,

$$\|\delta\boldsymbol{x}(t)\| \simeq \mathrm{e}^{\sigma t}\|\delta\boldsymbol{x}(0)\|. \tag{A.10}$$

Here the coefficient σ describes the average separation rate of nearby trajectories, and is often computed to indicate chaos. If this coefficient, called the *leading Lyapunov exponent* (LLE) is positive in the limit $t \to \infty$, then the orbit is called *chaotic*. A practical estimation of σ is given by simply solving (A.10) for σ, and approximating the infinite-time limit by some large time t i.e.,

$$\sigma \simeq \frac{1}{t}\ln\left\|\frac{\delta\boldsymbol{x}(t)}{\delta\boldsymbol{x}(0)}\right\|. \tag{A.11}$$

This computation of σ is carried out in practice by a method introduced by Wolf et al in [31], where the separation distances $\delta\boldsymbol{x}(t), \delta\boldsymbol{x}(0)$ are periodically re-normalized. More formally, for an n-dimensional dynamical system there are n Lyapunov exponents, defined in terms of the eigenvalues Λ_i of the Jacobian matrix $\mathbf{J}^k$,

$$\sigma_i \equiv \lim_{k\to\infty}\frac{1}{k}\ln|\Lambda_i|. \tag{A.12}$$

The existence of these limits are guaranteed for almost all points in the state space by the Oseledec Multiplicative Ergodic Theorem [33]. Since the leading Lyapunov exponent σ_1 will be the largest and therefore possess the the dominant corresponding eigendirection, in practice this exponent is sufficient to describe the separation rate. Thus, the above approximation for $\sigma_1 \equiv \sigma$ is just the result of approximating the tangent map by a finite difference.

Hamiltonian Systems – Area-preserving Maps

A dynamical system is named *Hamiltonian*[8] if it is completely described by a scalar function (the Hamiltonian) $H(\boldsymbol{q}, \boldsymbol{p}, t)$, defined by the Legendre transform of the Lagrangian function $\mathcal{L}$,

$$H \equiv \dot{\boldsymbol{q}} \cdot \boldsymbol{p} - \mathcal{L}, \tag{A.13}$$

where $\boldsymbol{q}$ denotes the generalized co-ordinates of the system, and the conjugate momenta $\boldsymbol{p}$ are defined in terms of the Lagrangian as $\boldsymbol{p} = \partial\mathcal{L}/\partial\dot{\boldsymbol{q}}$. The evolution of such a system is governed by Hamilton's equations

$$\dot{\boldsymbol{q}} = \frac{\partial H}{\partial \boldsymbol{p}}, \qquad \dot{\boldsymbol{p}} = -\frac{\partial H}{\partial \boldsymbol{q}}. \tag{A.14}$$

If the Hamiltonian has no explicit time dependence, the energy E, called the *first integral* or *constant of the motion*, is conserved. Examples of such systems include *undriven* dynamical billiards, such as the elliptical [35] and wedge [18] billiards. Additional constants of the motion can be found by identifying the momenta for which $\dot{p}_i = 0$ i.e., the momenta corresponding to co-ordinates which do not appear in the Hamiltonian. For a single particle in a constant field $\boldsymbol{g} = -g\hat{\boldsymbol{z}}$, the Hamiltonian is, in spherical co-ordinates,

$$H = \frac{1}{2m}\left(p_r^2 + \frac{1}{r^2}\left(p_\theta^2 + \frac{p_\phi^2}{\sin^2\theta}\right)\right) + gr\cos\theta \tag{A.15}$$

which makes the conservation of $p_\phi = \ell_z$, the z-component of angular momentum clear.

The continuous-time dynamics of Hamiltonian systems can be reduced to a discrete mapping in the usual fashion. The Poincaré surface-of-section (or Poincaré map for short) of a Hamiltonian system has the following feature: the map $\mathcal{P}$ is *area-preserving* i.e.,

$$\det \mathbf{J} = 1. \tag{A.16}$$

[8] For a more in-depth introduction to Hamiltonian systems, cf. for example [34].

This fact is useful in determining the stability of periodic orbits. In terms of the trace and determinant of $\mathbf{J}$, the eigenvalues of this matrix are

$$\lambda_{\pm} = \frac{\operatorname{Tr}\mathbf{J}}{2} \pm \sqrt{\frac{\operatorname{Tr}^2\mathbf{J}}{4} - \det\mathbf{J}}. \tag{A.17}$$

Hence the stability condition $|\lambda| < 1$ is equivalent to

$$|\operatorname{Tr}\mathbf{J}| < 2. \tag{A.18}$$

Dynamical Billiards

We define a *dynamical billiard* as the free motion of a particle inside a region $\mathcal{Q} \subset \mathbb{R}^n$ colliding with the boundary $\partial\mathcal{Q}$ [1]. At the boundary the billiard experiences specular reflections which preserves the tangential component of momentum and reverses the sign of the normal component i.e.,

$$\boldsymbol{p}^{+} = \boldsymbol{p}^{-} - 2(\boldsymbol{p}\cdot\boldsymbol{n})\boldsymbol{n}, \tag{A.19}$$

where $\boldsymbol{n}$ is a unit normal to the boundary $\partial\boldsymbol{Q}$. In general, for elastic collisions the Poincaré surface-of-section is $(2n-2)$-dimensional. For $n = 2$, traditionally the so-called *Birkhoff co-ordinates* are used, consisting of s, the arc length along $\partial\mathcal{Q}$ and p, the component of momentum parallel to $\partial\mathcal{Q}$ [35]. However, when a constant gravitational field is introduced the motion between collisions is no longer uniform, and the properties of these systems are more easily explored using more conventional co-ordinates.

Appendix B

Derivation of the Velocity Map for the Conic Billiard

From the fundamental definitions of spherical co-ordinates

$$\begin{aligned} x &= r\sin\theta\cos\phi, \\ y &= r\sin\theta\sin\phi, \\ z &= r\cos\theta, \end{aligned} \tag{B.1}$$

the unit vectors $\hat{\boldsymbol{r}}, \hat{\boldsymbol{\theta}}, \hat{\boldsymbol{\phi}}$ can be expressed as

$$\begin{aligned} \hat{\boldsymbol{r}} &= \sin\theta\cos\phi\hat{\boldsymbol{x}} + \sin\theta\sin\phi\hat{\boldsymbol{y}} + \cos\theta\hat{\boldsymbol{z}}, \\ \hat{\boldsymbol{\theta}} &= \cos\theta\cos\phi\hat{\boldsymbol{x}} + \cos\theta\sin\phi\hat{\boldsymbol{y}} - \sin\theta\hat{\boldsymbol{z}}, \\ \hat{\boldsymbol{\phi}} &= -\sin\phi\hat{\boldsymbol{x}} + \cos\phi\hat{\boldsymbol{y}}. \end{aligned} \tag{B.2}$$

from which the components of any vector $\boldsymbol{u}$ in the $\hat{\boldsymbol{r}}, \hat{\boldsymbol{\theta}}, \hat{\boldsymbol{\phi}}$ basis are obtained:

$$\begin{pmatrix} u_r \\ u_\theta \\ u_\phi \end{pmatrix} = \begin{pmatrix} \sin\theta\cos\phi & \sin\theta\sin\phi & \cos\theta \\ \cos\theta\cos\phi & \cos\theta\sin\phi & -\sin\theta \\ -\sin\phi & \cos\phi & 0 \end{pmatrix} \begin{pmatrix} u_x \\ u_y \\ u_z \end{pmatrix}. \tag{B.3}$$

The inverse transformation is

$$\begin{pmatrix} u_x \\ u_y \\ u_z \end{pmatrix} = \begin{pmatrix} \sin\theta\cos\phi & \cos\theta\cos\phi & -\sin\phi \\ \sin\theta\sin\phi & \cos\theta\sin\phi & \cos\phi \\ \cos\theta & -\sin\theta & 0 \end{pmatrix} \begin{pmatrix} u_r \\ u_\theta \\ u_\phi \end{pmatrix}. \tag{B.4}$$

Applying the collision equations

$$v^+_{n+1_r} = v^-_{n+1_r}, \qquad v^+_{n+1_\phi} = v^-_{n+1_\phi}, \qquad v^+_{n+1_\theta} = -v^-_{n+1_\theta}, \tag{B.5}$$

in terms of the Cartesian velocity components v_x, v_y, v_z results in a linear system of equations for the post-collision velocities $v^+_{n+1_x}, v^+_{n+1_y}$ and $v^+_{n+1_z}$ in terms of the corresponding pre-collision velocities $v^-_{n+1_x}, v^-_{n+1_y}$ and $v^-_{n+1_z}$. The solution of the system can be written

$$\begin{aligned}
v^+_{n+1_x} &= v^-_{n+1_x}(1 - 2\cos^2\phi_{n+1}\cos^2\theta) - v^-_{n+1_y}\sin 2\phi_{n+1}\cos^2\theta + v^-_{n+1_z}\cos\phi_{n+1}\sin 2\theta, \\
v^+_{n+1_y} &= -v^-_{n+1_x}\sin 2\phi_{n+1}\cos^2\theta + v^-_{n+1_y}(1 - 2\sin^2\phi_{n+1}\cos^2\theta) + v^-_{n+1_z}\sin\phi_{n+1}\sin 2\theta, \\
v^+_{n+1_z} &= v^-_{n+1_x}\cos\phi_{n+1}\sin 2\theta + v^-_{n+1_y}\sin\phi_{n+1}\sin 2\theta + v^-_{n+1_z}\cos 2\theta.
\end{aligned} \tag{B.6}$$

Since between collisions the billiard follows a simple parabolic trajectory, we have (recall that we set $g = \frac{1}{2}$ by a scaling transformation)

$$v^-_{n+1_x} = v_{n_x}, \qquad v^-_{n+1_y} = v_{n_y}, \qquad v^-_{n+1_z} = -\frac{\tau_{n+1}}{2} + v_{n_z}, \tag{B.7}$$

where $\tau_{n+1} \equiv t_{n+1} - t_n$. Using this in (B.6) and writing the Cartesian components of the velocity in terms of the spherical components (note that at the n^{th} collision the azimuthal angle is ϕ_n, and at the $n+1^{\text{th}}$ collision, ϕ_{n+1}), the velocity map becomes

(where we have abbreviated $v^+_{n+1_i} \equiv v_{n+1_i}$, and defined $\varphi_{n+1} \equiv \phi_{n+1} - \phi_n$)

$$v_{n+1_r} = v_{n_r}(\sin^2\theta\cos\varphi_{n+1} + \cos^2\theta) + v_{n_\theta}\sin\theta\cos\theta(\cos\varphi_{n+1} - 1) + v_{n_\phi}\sin\varphi_{n+1}\sin\theta - \frac{1}{2}\tau_{n+1}\cos\theta, \quad \text{(B.8)}$$

$$v_{n+1_\theta} = v_{n_r}\sin\theta\cos\theta(1 - \cos\varphi_{n+1}) - v_{n_\theta}(\cos^2\theta\cos\varphi_{n+1} + \sin^2\theta) - v_{n_\phi}\sin\varphi_{n+1}\cos\theta - \frac{1}{2}\tau_{n+1}\sin\theta, \quad \text{(B.9)}$$

$$v_{n+1_\phi} = -v_{n_r}\sin\varphi_{n+1}\sin\theta - v_{n_\theta}\sin\varphi_{n+1}\cos\theta + v_{n_\phi}\cos\varphi_{n+1}. \quad \text{(B.10)}$$

The difference in azimuthal angle φ_{n+1} is easily found to be given by

$$\varphi_{n+1} = \arctan\left(\frac{v_{n_\phi}\tau_{n+1}}{r_n\sin\theta + (v_{n_r}\sin\theta + v_{n_\theta}\cos\theta)\tau_{n+1}}\right),$$

and after some algebraic manipulation, together with the identities

$$\sin\arctan\left(\frac{a}{b}\right) = \frac{a}{\sqrt{a^2+b^2}}, \qquad \cos\arctan\left(\frac{a}{b}\right) = \frac{b}{\sqrt{a^2+b^2}}, \quad \text{(B.11)}$$

which imply

$$\sin\varphi_{n+1} = \frac{v_{n_\phi}\tau_{n+1}}{\sqrt{(r_n\sin\theta + (v_{n_r}\sin\theta + v_{n_\theta}\cos\theta)\tau_{n+1})^2 + v^2_{n_\phi}\tau^2_{n+1}}}$$
$$= \frac{v_{n_\phi}\tau_{n+1}}{\sqrt{((v_{n_r}\sin\theta + v_{n_\theta}\cos\theta)^2 + v^2_{n_\phi})\tau^2_{n+1} + 2r_n\sin\theta(v_{n_r}\sin\theta + v_{n_\theta}\cos\theta)\tau_{n+1} + r_n^2\sin^2\theta}}$$
$$= \frac{v_{n_\phi}\tau_{n+1}}{r_{n+1}\sin\theta}, \quad \text{(B.12)}$$

and similarly

$$\cos\varphi_{n+1} = \frac{r_n\sin\theta + (v_{n_r}\sin\theta + v_{n_\theta}\cos\theta)\tau_{n+1}}{r_{n+1}\sin\theta} = \frac{r_n + (v_{n_r} + v_{n_\theta}\cot\theta)\tau_{n+1}}{r_{n+1}}, \quad \text{(B.13)}$$

we find that the map for v_{n+1_r} is given by

$$\begin{aligned} v_{n+1_r} &= v_{n_r}\left(\sin^2\theta\frac{r_n+(v_{n_r}+v_{n_\theta}\cot\theta)\tau_{n+1}}{r_{n+1}}+\cos^2\theta\right) \\ &+ v_{n_\theta}\sin\theta\cos\theta\left(\frac{r_n+(v_{n_r}+v_{n_\theta}\cot\theta)\tau_{n+1}}{r_{n+1}}-1\right)+v_{n_\phi}\frac{v_{n_\phi}\tau_{n+1}}{r_{n+1}\sin\theta}\sin\theta-\frac{1}{2}\tau_{n+1}\cos\theta \\ &= \frac{\left((v_{n_r}\sin\theta+v_{n_\theta}\cos\theta)^2+v_{n_\phi}^2\right)\tau_{n+1}+r_n\sin\theta\,(v_{n_r}\sin\theta+v_{n_\theta}\cos\theta)}{r_{n+1}} \\ &\qquad + v_{n_r}\cos^2\theta-v_{n_\theta}\sin\theta\cos\theta-\frac{1}{2}\tau_{n+1}\cos\theta. \end{aligned} \tag{B.14}$$

In terms of the reduced variables

$$\rho\equiv r\sin\theta,\qquad u_r\equiv v_r\sin\theta,\qquad u_\theta\equiv v_\theta\cos\theta \tag{B.15}$$

the full (ρ,u_r) mapping becomes

$$\rho_{n+1}^2=\left[(u_{n_r}+u_{n_\theta})^2+\frac{\ell^2}{\rho_n^2}\right]\tau_{n+1}^2+2\rho_n\,(u_{n_r}+u_{n_\theta})+\rho_n^2, \tag{B.16}$$

$$\begin{aligned} u_{n+1_r} &= \frac{\sin^2\theta}{\rho_{n+1}}\left\{\left[(u_{n_r}+u_{n_\theta})^2+\frac{\ell^2}{\rho_n^2}\right]\tau_{n+1}+\rho_n\,(u_{n_r}+u_{n_\theta})\right\}+u_{n_r}\cos^2\theta-u_{n_\theta}\sin^2\theta \\ &\qquad -\frac{1}{4}\tau_{n+1}\sin 2\theta. \end{aligned} \tag{B.17}$$

The cubic equation for τ_{n+1}, in terms of these reduced variables, is

$$\begin{aligned} &\tau_{n+1}^3+8(u_{n_\theta}\tan\theta-u_{n_r}\cot\theta)\tau_{n+1}^2 \\ &\quad+16\left[(\sec^2\theta-\csc^2\theta)u_{n_\theta}^2-\frac{\ell^2\cot^2\theta}{\rho_n^2}-2u_{n_r}u_{n_\theta}\csc^2\theta-\frac{\rho_n\cot\theta}{2}\right]\tau_{n+1} \\ &\qquad -32\rho_n u_{n_\theta}\csc^2\theta=0. \end{aligned} \tag{B.18}$$

Bibliography

[1] G. D. Birkhoff. *Dynamical Systems.* American Mathematical Society, 1927.

[2] S. M. Ulam. On some statistical properties of dynamical systems. In *Proc. Fourth Berkeley Symp. on Math. Statist. and Prob.*, volume 3, pages 315–320, 1961.

[3] E. Fermi. On the origin of cosmic radiation. *Physical Review*, 75:1169, 1949.

[4] L. D. Pustyl'nikov. On a certain dynamical system. *Russian Math. Surveys*, 23, 1968.

[5] L. D. Pustyl'nikov. Existence of a set of positive measure of oscillating motions in a certain problem in dynamics. *Soviet Math. Dokl.*, 13:94, 1972.

[6] L. D. Pustyl'nikov. On the ulam problem. *Soviet Math. Dokl.*, 292:88, 1987.

[7] A. L. P. Livorati, D. G. Ladeira, and E. D. Leonel. Scaling investigation of fermi acceleration on a dissipative bouncer model. *Phys. Rev. E*, 78:056205, 2008.

[8] A. L. P. Livorati, T. Kroetz, C. P. Dettmann, I. L. Caldas, and E. D. Leonel. Stickiness in a bouncer model: A slowing mechanism for fermi acceleration. *Phys. Rev. E*, 86(3):036203, 2012.

[9] D. R. da Costa, C. P. Dettmann, and E. D. Leonel. Transport and dynamical properties for a bouncing ball model with regular and stochastic perturbations. *Comm. in Non. Sci. and Num. Sim.*, 20(3):871–881, 2015.

[10] A. Lichtenberg, M. Lieberman, and R. Cohen. Fermi acceleration revisited. *Physica D*, 1:291, 1980.

[11] P. J. Holmes. The dynamics of repeated impacts with a sinusoidally vibrating table. *Journal of Sound and Vibration*, 84(2):173, 1982.

[12] A. Lichtenberg and M. Lieberman. *Regular and Chaotic Dynamics*, volume 38 of *Applied Mathematical Sciences*. Springer New York, 1992.

[13] J. M. Luck and A. Mehta. Bouncing ball with a finite restitution: Chattering, locking, and chaos. *Phys. Rev. E*, 48:3988, 1993.

[14] M. A. Naylor, P. Sanchez, and P. Swift. Strange attractors of a bouncing ball. *Am. J. Phys.*, 55:316, 2002.

[15] S. Vogel and S. J. Linz. Regular and chaotic dynamics in bouncing ball models. *Int. J. of Bifurcation and Chaos*, 21(3):869, 2011.

[16] S. McNamara and W. R. Young. Inelastic collapse and clumping in a one-dimensional granular medium. *Phys. Fluids A*, 4(3), 1992.

[17] S. McNamara and W. R. Young. Inelastic collapse in two dimensions. *Phys. Rev. E*, 50(1), 1993.

[18] H. E. Lehtihet and B. N. Miller. Numerical study of a billiard in a gravitational field. *Physica D*, 21:93–104, 1986.

[19] P. H. Richter, H. J. Scholz, and A. Wittek. A breathing chaos. *Nonlinearity*, 3: 45–67, 1990.

[20] M. P. Wojtkowski. A system of one dimensional balls with gravity. *Comm. Math. Phys.*, 126:507–533, 1990.

[21] H. J. Korsch and J. Lang. A new integrable gravitational billiard. *J. Phys. A: Math. Gen.*, 24(45), 1991.

[22] M. L. Ferguson, B. N. Miller, and M. A. Thompson. Dynamics of a gravitational billiard with a hyperbolic lower boundary. *Chaos*, 9(4):841–848, 1999.

[23] S. Feldt and J. S. Olafsen. Inelastic gravitational billiards. *PRL*, 94(224102), 2005.

[24] A. E. Hartl, B. N. Miller, and A. P. Mazzoleni. Dynamics of a dissipative, inelastic gravitational billiard. *Phys. Rev. E*, 87(032901), 2013.

[25] F. Lenz, F. K. Diakonos, and P. Schmelcher. Classical dynamics of the time-dependent elliptical billiard. *Phys. Rev. E*, 76(066213), 2008.

[26] F. Lenz, C. Petri, F. K. Diakonos, and P. Schmelcher. Phase-space composition of driven elliptical billiards and its impact on fermi acceleration. *Phys. Rev. E*, 82 (016206), 2010.

[27] D. R. da Costa, C. P. Dettmann, and E. D. Leonel. Circular, elliptic and oval billiards in a gravitational field. *Comm. in Non. Sci. and Num. Sim.*, 22:731–746, 2015.

[28] A. Z. Gorski and T. Srokowski. Chaotic and regular motion in dissipative gravitational billiards. *Acta Physica Polonica B*, 37(2561), 2006.

[29] J. Hopkins and B. N. Miller. The gravitational bouncer and self-reanimating chaos. An unpublished algorithm used to safely determine the roots of a function which is the sum of a polynomial and a sinusoid.

[30] N. B. Tufillaro, T. Abbott, and J. P. Reilly. *An Experimental Approach to Nonlinear Dynamics and Chaos*. Addison-Wesley, 1992.

[31] A. Wolf, Swift. J. B., H. L. Swinney, and J. A. Vastano. Determining lyapunov exponents from a time series. *Physica D*, 16:285–317, 1985.

[32] Edward Ott. *Chaos in Dynamical Systems*. Cambridge University Press, 2002.

[33] V. I. Oseledec. A multiplicative ergodic theorem. liapunov characteristic numbers for dynamical systems. *Trans. Moscow Math. Soc.*, 19(197), 1968.

[34] J. H. Lowenstein. *Essentials of Hamiltonian Dynamics*. Cambridge University Press, 2012.

[35] M. V. Berry. Regularity and chaos in classical mechanics, illustrated by three deformations of a circular 'billiard'. *Eur. J. Phys.*, 2:91–102, 1981.